THE ASTROPHYSICAL JOURNAL, 411:614–631, 1993 July 10

MULTIWAVELENGTH MONITORING OF THE BL LACERTAE OBJECT PKS 2155−304. I. THE *IUE* CAMPAIGN

C. M. URRY,[1,2] L. MARASCHI,[2,3] R. EDELSON,[4] A. KORATKAR,[1] J. KROLIK,[5] G. MADEJSKI,[4,6] E. PIAN,[7] G. PIKE,[4] G. REICHERT,[4,6] A. TREVES,[7] W. WAMSTEKER,[8] R. BOHLIN,[1] J. BREGMAN,[9] W. BRINKMANN,[10] L. CHIAPPETTI,[11] T. COURVOISIER,[12] A. V. FILIPPENKO,[13] H. FINK,[10] I. M. GEORGE,[4] Y. KONDO,[14] P. G. MARTIN,[15,16] H. R. MILLER,[17] P. O'BRIEN,[18] J. M. SHULL,[19] M. SITKO,[20] A. E. SZYMKOWIAK,[4] G. TAGLIAFERRI,[21] S. WAGNER,[22] AND R. WARWICK[23]

Received 1992 November 24; accepted 1993 January 7

ABSTRACT

Daily monitoring of PKS 2155−304 with the *IUE* satellite throughout 1991 November has revealed dramatic, large-amplitude, rapid variations in the ultraviolet flux of this BL Lac object. Many smaller, rapid flares are superposed on a general doubling of the intensity. During the 5^d period when sampling was roughly continuous, the rapid flaring had an apparent quasi-periodic nature, with peaks repeating every $\sim 0^d.7$. The short- and long-wavelength ultraviolet light curves are well correlated with each other, and with the optical light curve deduced from the Fine Error Sensor (FES) on *IUE*. The formal lag is zero, but the cross-correlation is asymmetric in the sense that the shorter wavelength emission leads the longer. The ultraviolet spectral shape varies a small but significant amount. The correlation between spectral shape and intensity is complicated; an increase in intensity is associated with spectral hardening, but lags behind the spectral change by ~ 1 day. The sign of the correlation is consistent with the nonthermal acceleration processes expected in relativistic plasmas, so that the present results are consistent with relativistic jet models, which can also account for quasi-periodic flaring. In contrast, currently proposed accretion disk models are strongly ruled out by the simultaneous optical and ultraviolet variability.

Subject headings: BL Lacertae objects: individual (PKS 2155−304) — galaxies: active — ultraviolet: galaxies

1. INTRODUCTION

The most puzzling aspect of active galactic nuclei (AGNs) has always been their high power output coupled with the small emission region inferred from rapid variability. The characteristics shared by the most rapidly variable objects, BL Lac objects and optically violently variable (OVV) quasars, collectively called "blazars," such as high (and variable) polarization, compact radio structure, a smooth continuum spectrum from radio through soft X-ray wavelengths, and superluminal motion, may owe their origin to a relativistic jet (Blandford & Rees 1978). The unreasonably high inferred radio brightness temperatures ($T \gg 10^{12}$ K; Quirrenbach et al. 1989) and flare quotients in excess of the Eddington-limited value assuming accretion efficiency η (Fabian 1979), $\Delta L/\Delta t > 2 \times 10^{42}\ \eta$ ergs s^{-2} (e.g., Feigelson et al. 1986; Morini et al. 1986), often exhibited by blazars, can most easily be explained by relativistic effects. The quantity $\Delta L/\Delta t$ is proportional to δ^5, where $\delta = (\gamma[1 - \beta \cos \theta])^{-1}$ is the kinematic Doppler factor describing relativistic motion with Lorentz factor γ (velocity β) at an angle θ to the line of sight.

In the last decade, considerable progress has been made interpreting the broad-band spectra of blazars in terms of models of inhomogeneous relativistic jets (Marscher 1980; Königl 1981; Ghisellini, Maraschi, & Treves 1985; Worrall et al. 1986; Hutter & Mufson 1986; George, Warwick, & Bromage 1988). These models have been very successful, in the sense that with a minimal number of parameters they usually fit the continuum spectrum over nearly 10 decades in wavelength. Unfortunately, the parameters of the model are rarely well determined because a variety of assumptions can produce acceptable fits for a large volume of parameter space. The degeneracy of multiple model solutions vanishes or is greatly

[1] Space Telescope Science Institute, 3700 San Martin Drive, Baltimore, MD 21218.
[2] Guest Observer with the *International Ultraviolet Explorer*.
[3] Department of Physics, University of Milan, via Celoria 16, I-20133 Milan, Italy.
[4] Laboratory for High Energy Astrophysics, Code 660, NASA/GSFC, Greenbelt, MD 20771.
[5] The Johns Hopkins University, Department of Physics and Astronomy, Baltimore, MD 21218.
[6] Universities Space Research Association, Code 610.3, NASA/GSFC, Greenbelt, MD 20771.
[7] SISSA/ISAS International School for Advanced Studies, Trieste, Italy.
[8] ESA *IUE* Observatory, P.O. Box 50727, 28080 Madrid, Spain.
[9] Department of Astronomy, Dennison Building, University of Michigan, Ann Arbor, MI 48109.
[10] MPE, Giessenbachstrasse, D-8046 Garching bei München, Germany.
[11] Istituto di Fisica Cosmica CNR, via Bassini 15, I-20133 Milan, Italy.
[12] Observatory of Geneva, Ch-1290 Sauverny, Switzerland.
[13] Department of Astronomy, University of California, Berkeley, CA 94720.
[14] Laboratory for Astronomy and Solar Physics, NASA/GSFC, Greenbelt, MD 20771.
[15] Canadian Institute for Theoretical Astrophysics, University of Toronto, Ontario M5S 1A7.
[16] Also, Theoretical Astrophysics, 130-33, Caltech, Pasadena, CA 91125.
[17] Department of Physics, Georgia State University, Atlanta, GA 30303.
[18] Department of Physics and Astronomy, University College London, Gower Street, London WC1E 6BT, England.
[19] JILA, University of Colorado, and National Institute of Standards and Technology, Campus Box 440, Boulder, CO 80309.
[20] Department of Physics, University of Cincinnati, 210 Braunstein M1 11, Cincinnati, OH 45221.
[21] Osservatorio Astronomico di Brera, Via Brera 28, 20121 Milan, Italy.
[22] Landessternwarte Heidelberg-Königstuhl, D-6900 Heidelberg 1, Germany.
[23] Department of Physics, University of Leicester, University Road, Leicester LE1 7RH, England.

reduced when variability information is added because the change in spectrum with intensity is a strong diagnostic of the emission process (e.g., George et al. 1988; Mufson et al. 1990). However, the sampling available to date—only a few spectra, spaced far apart in time—has been sparse, uneven, and inadequate.

Inhomogeneous jet models are strongly supported by radio and optical observations, but the situation at higher frequencies is less clear. Alternatives include a two-temperature accretion disk model (Wandel & Urry 1991) and gravitational microlensing of background quasars (Ostriker & Vietri 1985, 1990; Stickel, Fried, & Kühr 1988; Schneider & Weiss 1987). The disk and jet models differ most at ultraviolet through X-ray wavelengths, where the spectral curvature is greatest; among jet models there are differences in how the ultraviolet and X-ray emission are related (e.g., Ghisellini et al. 1985). Simultaneous, multiwavelength, well-sampled light curves are ideal for testing the models. The amplitude and rapidity of variability in most blazars increases with decreasing wavelength, so the chances of successfully observing significant variations at ultraviolet and soft X-ray wavelengths are high. As other monitoring programs (with the different goal of mapping the broad emission-line regions in nonblazar AGNs) have clearly demonstrated (e.g., Clavel et al. 1991), the *IUE* observatory is very well suited to regular monitoring of AGNs because of its ease of scheduling, efficient geosynchronous orbit, precise photometric calibration and stability, and broad wavelength coverage.

We designed a monitoring program that would produce high-quality light curves in several bands, including unprecedented spectral coverage in the ultraviolet, extreme ultraviolet, and soft-X-ray from the combination of *IUE*, the *ROSAT* Wide Field Camera (WFC), and the *ROSAT* Position Sensitive Proportional Counter. The object selected for our study, PKS 2155−304, is one of the brightest extragalactic objects in the ultraviolet and X-ray sky. Like most BL Lac objects, PKS 2155−304 has no strong emission features; the reported redshift of $z = 0.117$ (Bowyer et al. 1984) is probably due to a galaxy displaced $\sim 4''$ from the BL Lac object, but a redshift of ~ 0.1 can be inferred from imaging of the host galaxy (Falomo et al. 1991). PKS 2155-304 has previously been observed to be highly variable at both ultraviolet (Maraschi et al. 1986; Urry et al. 1988; Edelson et al. 1991) and X-ray (Snyder et al. 1980; Sembay et al. 1992) wavelengths, with some evidence of quasi-simultaneous variability in those bands, albeit with smaller amplitudes and longer time scales at the longer wavelengths (Treves et al. 1989). The soft X-ray spectrum is steep and can be connected smoothly to the ultraviolet spectrum, implying that the ultraviolet and X-ray emission mechanisms may be related. This motivated the first application of relativistic jet (Urry & Mushotzky 1982) and accretion disk (Wandel & Urry 1991) models to the continuum emission from PKS 2155−304.

In 1990, proposals to observe PKS 2155−304 were submitted to *IUE* (one to NASA, one to ESA) and to *ROSAT* (a U.S. proposal for month-long daily monitoring which was unsuccessful and a German proposal for intensive monitoring over a few days). PKS 2155−304 is bright enough to be observed easily in a half-*IUE* shift (4 hr) or once per *ROSAT* orbit (roughly 2000 s). This paper describes the *IUE* data set, which is of unprecedented quality. Associated observations at other wavelengths are being reported separately, including month-long ground-based optical, infrared, and radio monitoring (Smith et al. 1992; Courvoisier et al. 1993), quasi-continuous 4^d *ROSAT* observations (Brinkmann et al. 1993), and multiwavelength cross-correlations (Edelson et al. 1993). The *IUE* observations and data analysis are described in § 2 of this paper, followed by the results in § 3. The implications of the ultraviolet variability for models of blazars are discussed in § 4, and the conclusions are summarized in § 5.

2. OBSERVATIONS AND DATA ANALYSIS

2.1. *Observing Strategy*

The *ROSAT* spacecraft constraints restricted observing to a 32 day period from 1991 October 27 to 1991 November 28, so the monitoring campaign was planned for that time. (In the end, *ROSAT* monitored the source only for a few days in the middle of the month; Brinkmann et al. 1993.) The variability time scales of BL Lac objects in general, and even this best studied object PKS 2155−304 in particular, were not well measured previously, so the observing plan bracketed a range of time scales. In order to measure moderate time scale variations (days to a week) we scheduled at least one-half *IUE* shift daily from November 1 to November 29 (except on November 8, due to a scheduling conflict). In order to study short-term variability, $4^d.6$ in the middle of the campaign (November 10.7–15.3) were devoted to nearly continuous coverage using about three shifts per day. A log of the 201 *IUE* observations is given in Table 1.

The short-wavelength (SWP) and long-wavelength (LWP) *IUE* cameras were exposed alternately, with nominal integration times of 55 and 25 minutes, respectively. This allowed us to get two pairs of spectra during each half-*IUE* shift, in the absence of any operational problems. Just before each SWP or LWP exposure, counts from the Fine Error Sensor (FES), the optical monitor on *IUE*, were measured on target and on background. During the continuous observing period, the SWP/LWP/FES observing cycle was slaved to the 95.8 minute *ROSAT* orbital period so that the *IUE* and *ROSAT* observations would be locked in phase, thus greatly simplifying the cross-correlation between ultraviolet and X-ray light curves. As a result of this rigid schedule, some *IUE* exposures had to be longer or shorter than the nominal exposure times, typically by a few minutes but occasionally by much more. Exposure times for each *IUE* image are listed in Table 1.

2.2. *Optical Calibration*

The FES counts were converted to optical magnitudes using the recently developed algorithm of Perez & Loomis (1991), which takes into account the background due to scattered light. PKS 2155−304 was assumed to have color $B-V = 0.26$ mag throughout the month, which is the mean value measured contemporaneously with ground-based optical telescopes (it did not change much during the monitoring period; Smith et al. 1992). In any case, the conversion from FES counts to V magnitude is not terribly sensitive to the color; for example, using $B-V = 0.5$ mag would increase V by about 0.06 mag. Reddening corrections are minimal at these wavelengths (well within the FES accuracy), and so were ignored. The FES-derived V magnitudes are given in Table 1, and the optical light curve is discussed in § 3.1.

2.3. *Ultraviolet Spectral Extraction*

Spectra were extracted from each of the 201 *IUE* images using the Slit-Weighted Extraction Technique (SWET) of Kinney, Bohlin, & Neill (1991). Note that SWET-extracted

1993ApJ...411..614U

TABLE 1

LOG OF *IUE* OBSERVATIONS OF PKS 2155−304

IUE Image	Start Time (UT) (Day of Nov 91)	Exposure Time (min)	V Magnitude (from FES counts)	Observatory (Goddard or Vilspa)
LWP21607	1.832	30	13.29	G
SWP42969	1.860	55	13.29	G
LWP21608	1.905	30	13.29	G
SWP42970	1.930	55	13.34	G
LWP21609	1.971	25	13.24	G
SWP42971	1.993	55	13.33	G
LWP21610	2.036	25	13.26	G
SWP42972	2.059	55	13.25	G
LWP21611	2.101	25	13.29	G
LWP21616	2.825	25	13.18	G
SWP42979	2.847	55	13.15	G
LWP21617	2.889	25	13.18	G
SWP42980	2.913	55	13.29	G
LWP21625	3.834	25	13.18	G
SWP42995	3.857	55	13.15	G
LWP21626	3.905	25	13.18	G
SWP42996	3.929	35	13.20	G
LWP21636	4.817	25	12.99	G
SWP43008	4.842	55	12.98	G
LWP21637	4.888	25	12.99	G
SWP43009	4.913	55	13.02	G
LWP21644	5.828	25	13.03	G
SWP43017	5.853	55	12.97	G
LWP21645	5.903	25	12.95	G
SWP43018	5.928	55	12.94	G
LWP21652	6.813	25	—	G
SWP43025	6.985	55	13.05	G
LWP21653	7.031	25	13.05	G
SWP43026	7.056	55	13.08	G
LWP21654	7.103	25	13.08	G
LWP21667	9.041	25	12.94	G
SWP43040	9.177	55	12.96	G
LWP21668	9.224	25	12.89	G
SWP43041	9.252	55	12.92	G
LWP21673	9.675	25	12.86	V
SWP43047	9.700	55	12.85	V
LWP21674	9.742	25	12.89	V
SWP 43048[a]	9.765	25	12.85	V
LWP21683	10.663	25	12.83	V
SWP43054	10.685	55	12.81	V
LWP21684	10.728	25	12.87	V
SWP43055	10.751	55	12.78	G
LWP21685	10.797	25	12.76	G
SWP43056	10.821	51	12.84	G
LWP21686	10.864	25	12.81	G
SWP43057	10.886	55	12.80	G
LWP21687	10.929	25	12.76	G
SWP43058	10.953	52	12.80	G
LWP21688	10.996	25	12.79	G
SWP43059	11.018	55	12.77	G
LWP21689	11.062	25	12.75	G
SWP43060	11.085	52	12.77	G
LWP21690	11.128	25	12.75	G
SWP43061	11.152	51	12.76	G
LWP21691	11.195	23	12.72	G
SWP43062	11.219	51	12.74	G
LWP21692	11.260	25	12.70	G
SWP43063	11.285	55	12.72	G
LWP21693	11.328	25	12.70	G
SWP43064	11.353	50	12.71	G
SWP43065	11.815	57	12.73	G
LWP21696	11.862	25	—	G
SWP43066	11.889	45	12.69	G
LWP21697	11.924	27	12.69	G
SWP43067	11.947	58	12.66	G
LWP21698	11.993	25	—	G
SWP43068	12.014	57	12.68	G
LWP21699	12.058	27	12.68	G
SWP43069	12.081	57	12.68	G
LWP21700	12.125	27	12.66	G
SWP43070	12.150	54	12.72	G
LWP21701	12.192	25	12.66	G
SWP43071	12.215	55	12.70	G
LWP21702	12.258	28	12.72	G
SWP 43073[a]	12.510	13	12.74	V
LWP21704	12.525	25	12.84	V
SWP43074	12.549	55	12.73	V
LWP21705	12.592	25	12.65	V
SWP43075	12.615	55	12.70	V
LWP21706	12.658	25	12.73	V
SWP43076	12.686	49	12.73	V
LWP21707	12.725	25	12.69	V
SWP43077	12.748	55	12.63	G
LWP21708	12.791	25	12.68	G
SWP43078	12.814	55	12.68	G
LWP21709	12.858	25	12.69	G
SWP43079	12.880	55	12.69	G
LWP21710	12.922	28	12.72	G
SWP43080	12.946	57	12.69	G
LWP21711	12.991	25	12.73	G
SWP43081	13.015	53	12.78	G
LWP21712	13.061	25	12.73	G
SWP43082	13.083	51	12.75	G
LWP21713	13.123	25	12.74	G
SWP43083	13.150	51	12.75	G
LWP21714	13.189	25	12.72	G
SWP43084	13.212	55	12.75	G
LWP21715	13.258	25	12.72	G
SWP43085	13.280	55	12.75	G
LWP21716	13.322	25	12.78	G

TABLE 1—*Continued*

IUE Image	Start Time (UT) (Day of Nov 91)	Exposure Time (min)	V Magnitude (from FES counts)	Observatory (Goddard or Vilspa)	IUE Image	Start Time (UT) (Day of Nov 91)	Exposure Time (min)	V Magnitude (from FES counts)	Observatory (Goddard or Vilspa)
SWP43086	13.343	65	12.81	G	LWP21748	16.232	25	12.64	G
SWP 43088[a]	13.498	27	12.73	V	SWP43115	16.254	40	12.64	G
LWP21717	13.523	25	12.75	V	LWP21755	16.821	25	12.66	G
SWP43089	13.554	42	12.76	V	SWP43121	16.841	55	12.66	G
LWP21718	13.590	25	12.80	V	LWP21756	16.882	25	12.61	G
SWP43090	13.612	55	12.71	V	SWP43122	16.903	65	12.64	G
LWP21719	13.656	25	12.82	V	LWP21768	17.819	25	12.73	G
SWP43091	13.679	55	12.84	V	SWP43135	17.841	55	12.68	G
LWP21720	13.723	25	12.83	V	LWP21769	17.883	25	12.67	G
SWP43092	13.748	52	12.84	G	SWP43136	17.908	60	12.68	G
LWP21721	13.788	26	12.80	G	SWP43145	18.815	55	12.74	G
SWP43093	13.811	56	12.78	G	LWP21777	18.859	27	12.76	G
LWP21722	13.854	27	12.86	G	SWP43146	18.884	55	12.74	G
SWP43094	13.877	57	12.88	G	LWP21778	18.928	33	12.73	G
LWP21723	13.921	27	12.87	G	LWP21786	20.014	25	12.73	G
SWP43095	13.948	52	12.91	G	SWP43157	20.035	55	12.78	G
LWP21724	13.988	27	12.87	G	LWP21787	20.078	27	12.81	G
SWP43096	14.011	57	12.89	G	SWP43158	20.103	33	12.79	G
LWP21725	14.054	27	12.91	G	SWP43164	20.695	55	12.69	V
SWP43097	14.077	57	12.91	G	LWP21793	20.740	25	12.69	V
LWP21726	14.121	27	12.89	G	SWP 43165[a]	20.766	25	12.69	V
SWP43098	14.144	57	12.87	G	SWP43174	21.673	55	12.69	V
LWP21727	14.189	25	12.64	G	LWP21799	21.718	25	12.74	V
SWP43099	14.213	53	12.86	G	SWP43175	21.747	55	12.65	V
LWP21728	14.255	30	12.80	G	SWP43184	22.662	55	12.60	V
LWP21730	14.521	25	12.87	V	LWP21810	22.707	25	—	V
SWP43101	14.544	55	12.84	V	SWP43185	22.730	47	12.76	V
LWP21731	14.587	25	12.79	V	LWP21811	22.767	25	—	V
SWP43102	14.610	55	12.77	V	SWP43192	23.683	55	12.59	V
LWP21732	14.654	25	12.83	V	LWP21828	23.729	25	12.68	V
SWP43103	14.681	49	12.77	V	SWP43193	23.753	44	12.60	V
LWP21733	14.721	25	12.71	V	SWP 43211[b]	24.684	55	12.78	V
SWP43104	14.744	55	12.79	G	LWP 21837[b]	24.750	32	12.73	V
LWP21734	14.786	27	12.69	G	SWP43220	25.679	55	12.83	V
SWP43105	14.810	55	12.74	G	LWP21847	25.723	25	12.77	V
LWP21735	14.852	27	12.72	G	SWP43221	25.749	50	12.79	V
SWP43106	14.875	57	12.75	G	SWP43230	26.678	55	12.58	V
LWP21736	14.919	27	12.70	G	LWP21856	26.724	25	12.54	V
SWP43107	14.942	57	12.73	G	SWP43231	26.751	45	12.56	V
LWP21737	14.985	27	12.74	G	SWP43236	27.677	55	12.59	V
SWP43108	15.009	57	12.75	G	LWP21864	27.725	25	12.56	V
LWP21738	15.051	27	12.74	G	SWP43237	27.747	50	12.54	V
SWP43109	15.074	58	12.71	G	LWP21877	28.832	25	11.82	G
LWP21739	15.119	27	12.72	G	SWP43246	28.858	45	12.59	G
SWP43110	15.144	54	12.77	G	LWP21878	28.895	25	12.61	G
LWP21740	15.185	27	12.78	G	SWP43247	28.919	45	12.62	G
SWP43111	15.207	57	12.73	G	SWP43260	29.824	55	12.55	G
LWP21741	15.250	35	12.72	G	LWP21888	29.867	25	12.58	G
LWP21744	15.816	25	12.77	G	SWP43261	29.893	50	12.61	G
LWP21747	16.168	25	12.71	G	LWP21889	29.932	25	12.57	G
SWP43114	16.190	55	12.67	G					

Notes — [a]Unusually short exposure time; [b]Interrupted exposure

spectra are the standard output for low-dispersion images in the Final *IUE* Archive that is now being created jointly by NASA, ESA, and SERC (the British Science and Engineering Research Council). The current IUESIPS software still uses a boxcar extraction, but the SWET software is publicly available through the *IUE* Regional Data Analysis Facility and has been incorporated into a number of processing pipelines, including our own.

Details of the SWET procedure can be found in Kinney et al. (1991), and we merely summarize the major points here. Empirical spline fits are made to the cross-dispersion point spread function (PSF) along the spectrum, which constrains the PSF to vary smoothly in the dispersion direction. This imposition of information contributes to an improvement in the signal-to-noise ratio of the extracted spectrum relative to IUESIPS, while flux is still conserved. The flux at each wavelength is then determined by fitting the empirically determined profile, sample by sample, weighted according to a noise model determined from studies of hundreds of unrelated *IUE* images. Discrepant points are eliminated, which automatically removes most of the cosmic rays, with the exception of those that fall exactly at the center of the cross-dispersion profile. An uncertainty is associated with each flux value based on the noise model. Extensive comparisons of SWET-extracted and boxcar-extracted spectra show no systematic disagreement between the two (Kinney et al. 1991).

There is another well-known slit-weighted technique, the Gaussian extraction or GEX method (Urry & Reichert 1988), which assumes the cross-dispersion profile is a Gaussian. Because of this additional constraint, GEX gives a somewhat better signal-to-noise ratio than SWET for very low signal-to-noise ratio data, but for well-exposed spectra, systematic problems at the level of a few percent can occur because the true PSF is not precisely Gaussian. In the present case, the spectra are generally well exposed, so that the SWET method is slightly preferred to the automatic GEX algorithms currently available, which in any case do not produce an error vector. Nonetheless, we have also extracted all the spectra using GEX, and compared this to the SWET results. Although there are small systematic differences between spectra extracted with the two extraction methods, the results (which depend on fitted fluxes; see § 2.5) are not affected significantly (see § 3.4).

2.4. *Ultraviolet Spectral Corrections*

The extracted net fluxes were converted to absolute flux using the *IUE* calibration of Bohlin et al. (1990), which produces absolute fluxes that are up to 10% smaller than the white dwarf calibration (Finley et al. 1993) being used for the *IUE* Final Archive. A correction was made for degradation in the SWP sensitivity (Bohlin & Grillmair 1988, as updated through 1989.36 by R. Bohlin, private communication). The extrapolation to 1992 introduces some noise on the 5 Å scale but should not cause absolute flux errors of more than 1% in broad bands. No sensitivity correction was made to the LWP net flux.

We then considered a reddening correction. The column density of hydrogen through the interstellar medium of our Galaxy toward PKS 2155−304, as measured with the 2° × 3° beam 21 cm survey of Stark et al. (1992), is $N_{\rm H\,I} = 1.78 \times 10^{20}$ atoms cm^{-2}. Using an *IUE*-based average conversion of $\log N_{\rm H\,I}/E(B-V) = 21.72 \pm 0.26$ cm^{-2} mag^{-1} (Shull & Van Steenberg 1985), this corresponds to $E(B-V) \sim 0.034$ mag, with large uncertainties (discussed in detail in § 3.4). The actual line-of-sight column density could be different due to small-scale, high-latitude fluctuations (e.g., Elvis, Lockman, & Wilkes 1989), but the soft X-ray spectrum of PKS 2155−304 is consistent with this column density of absorbing cool gas (e.g., Canizares & Kruper 1984; Madejski 1985), as are results from the Hopkins Ultraviolet Telescope, which is sensitive down to 912 Å (J. Kruk, private communication). These results all indicate there is little or no internal reddening in PKS 2155−304.

The *IUE* spectra were dereddened using $E(B-V) = 0.034$ mag and the average Galactic curve from Seaton (1979). The dereddening correction has often been ignored by previous *IUE* observers of PKS 2155−304, ourselves included, but it makes a significant difference. The dereddened flux is 31% greater at 1400 Å and 21% greater at 2800 Å than the observed flux, and the fitted energy spectral index is typically 0.07 flatter in the SWP and 0.32 flatter in the LWP.[24] Because the amount of dereddening is uncertain, the absolute ultraviolet luminosity is uncertain, but this remains true whether or not the dereddening correction is applied.

Since we are interested in the source properties unmodified by the accident of transmission through our Galaxy, further discussion focuses on the dereddened spectra, keeping in mind that the amount of reddening is uncertain. The accuracy of the assumed Galactic reddening is considered further in § 3.4.

2.5. *Ultraviolet Spectral Fitting*

Using an iterative, χ^2 minimization fitting routine, the dereddened *IUE* spectra were fitted to a simple power-law model for the form

$$F_\lambda = b_1 \left(\frac{\lambda}{\lambda_0}\right)^{b_2} . \quad (1)$$

The fit parameters are the normalization, b_1, at fiducial wavelength λ_0, and the slope, b_2. The definition of power-law slope seen most often in the literature is the energy index, α, where $F_\nu \propto \nu^{-\alpha}$, which is related to b_2 via $\alpha = 2 + b_2$. The results are given here in terms of the energy index, α, but the fitting was done in wavelength space, with no resampling to frequency space.

Two sample fits to the data, chosen to be representative of the median intensities and the mean χ^2_ν values for the SWP and LWP samples as a whole, are shown in Figure 1; the SWET error vectors are plotted below each spectrum. (In order to show the raw extracted spectra, the data and fits in Fig. 1 are not dereddened.) The wavelength ranges over which the data were fitted were 1230–1950 Å for the SWP camera (which excludes the geocoronal Lyman-α region) and 2100–3100 for the LWP camera. Wavelength regions affected by SWP camera artifacts (Crenshaw, Bruegman, & Norman 1990), at 1277–1281 Å, 1286–1290 Å, and 1660–1666 Å, were excluded, as was the region 1470–1540 Å, in which unusual features were apparent in many of the spectra. These excluded regions are shown as light dotted lines in Figure 1*a*. Since the artifacts in the LWP camera are of low contrast, no spectral regions were excluded in those fits. The power-law fit is clearly good, as is generally true for all the spectra.

[24] The effect of reddening is greatest at the shortest wavelengths, but the change in spectral index is actually greater in the LWP band than in the SWP band because the slope of the reddening curve over the heavily weighted part of the LWP band is larger than the slope in the SWP band.

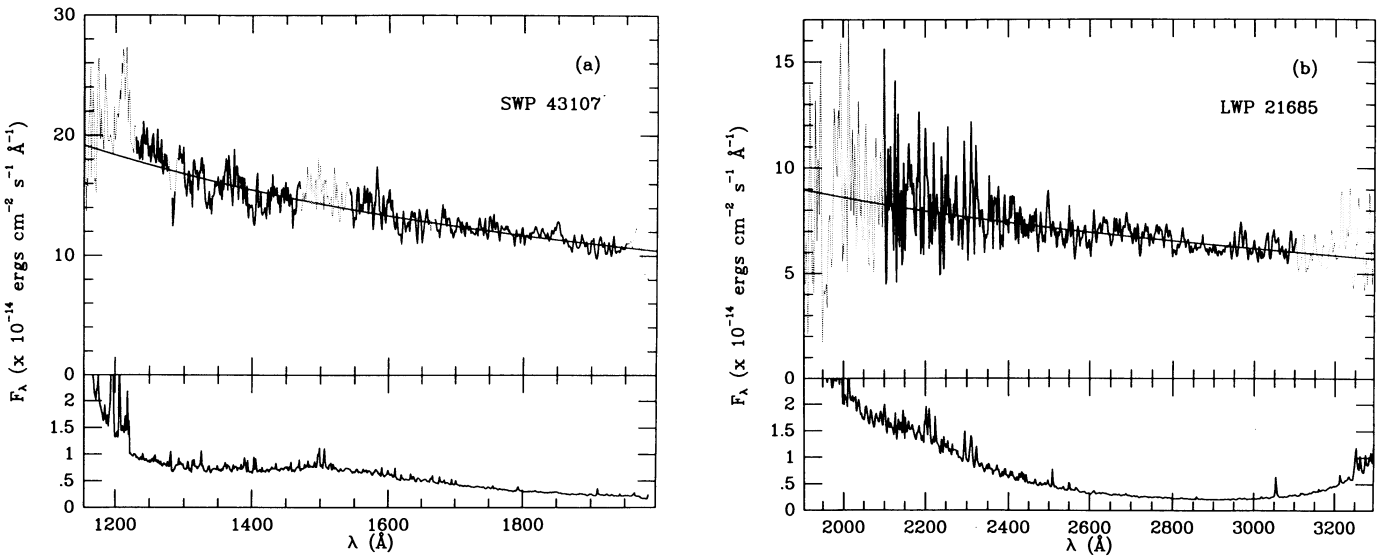

FIG. 1.—Representative spectra from among the 201 spectra in the data set. In both cases the source intensities are approximately the median values for the month-long monitoring campaign, and the exposure times are typical. Regions excluded from the power-law fitting are shown as dotted lines. Best-fit power law models, weighted according to the SWET error vector plotted in the panel at bottom, are shown as smooth curves; the spectra have not been dereddened, so the fits shown differ from those presented in Table 2. (*a*) An SWP spectrum obtained on 1991 November 14, with $\chi_\nu^2 = 3.44$ for the best-fit power-law model. (*b*) An LWP spectrum obtained on 1991 November 10, with $\chi_\nu^2 = 2.25$ for the best-fit power law.

Results of the fits to dereddened spectra are given in Table 2. The normalization is at 1400 Å for SWP spectra and 2800 Å for LWP spectra (as in Edelson et al. 1992). These wavelengths are close to the flux-weighted means of each band (∼1560 Å and ∼2568 Å, respectively, for $\alpha = 1$), so that the uncertainty in the derived flux is small; they are in regions of the cameras where the signal-to-noise ratio is good; and they were chosen to be relatively far away from one another, increasing the independence of the SWP and LWP flux measurements. The reduced χ^2 values in Table 2 were calculated using the raw SWET errors, prior to the correction procedure described in the next section.

We also fitted combined spectra, which is to say pairs of SWP and LWP spectra taken close together in time, spliced together at 1978 Å. Power laws were fitted to the wavelength range 1230–3100 Å, excluding the same regions as in the SWP analysis above, as well as 1900–2150 Å (which has relatively large errors anyway). The results are given in Table 3. The advantage of fitting combined SWP-LWP spectra is that the longer baseline in wavelength gives smaller uncertainties on the fitted flux and spectral index; however, the mismatch between SWP and LWP spectra seen in previous work (e.g., Urry et al. 1988; George et al. 1988) and again here (see § 3.3) illustrates how the absolute values of fitted flux and spectral index depend on the uncertain intercalibration of the two cameras. Therefore, for absolute values of the flux and spectral index, the estimates from fits to the individual spectra (F_{1400}, F_{2800}, α_{SWP}, and α_{LWP}, in Table 2) are better than those from the combined fits (α_C and F_C, in Table 3). We consider the latter quantities when evaluating *changes* in spectral shape and intensity because of the larger bandwidth for the power-law fits (the combined spectral index is an effective hardness ratio between the SWP and LWP cameras).

2.6. *Error Analysis*

Estimating the error bars reliably is the key to the detection and evaluation of variability. *IUE* spectra are dominated by systematic noise, including well-known features at the wavelengths mentioned above. A continuum estimate from direct measurement would have a relatively large error bar (the variance in some interval around that wavelength), including both local statistical noise and fixed-pattern noise. Like most BL Lac objects, however, PKS 2155−304 has a smooth and approximately featureless spectrum which is well fitted by a simple power-law model. The flux calculated from a fitted power law gives a much smaller error bar than direct measurement because information from the full band is used.

The initial estimate of the uncertainty in the flux measurement comes directly from propagated uncertainties on fit parameters. The latter are derived from the error matrix calculated in the least-squares fitting procedure (e.g., Bevington 1969), which in turn depends linearly on the SWET errors used to weight the input data points. Thus, the estimated uncertainty in the flux measurement scales linearly with any modification to the SWET error.

While the relative sizes of the SWET errors make sense, the χ^2 distribution for the 201 spectral fits is far from acceptable. The mean reduced χ^2 values for the SWP and LWP fits are $\langle\chi_\nu^2\rangle = 3.76$ and $\langle\chi_\nu^2\rangle = 2.42$, respectively, where the number of degrees of freedom is taken as the number of points fitted in the spectrum (539 and 535, respectively) minus the number of fit parameters (two). The probability of exceeding either of these values given the number of degrees of freedom is vanishingly small. The power-law model appears to be a good fit to the data, and there are no systematic trends in the residuals that would indicate a different model might be preferred, so either the SWET errors are underestimated or the number of degrees of freedom (the number of independent points in each spectrum) is overestimated.

Previous authors (e.g., Clavel et al. 1991) have suggested normalizing the error vector for a given spectrum by the square root of the reduced χ^2 value for that fit. In our view this is not the best approach, as it makes the χ_ν^2 distribution for all the fits look like a delta-function when in fact the χ_ν^2 values

TABLE 2

POWER-LAW FITS TO DEREDDENED SPECTRA

IUE Image	Observation Midpoint (UT) (Day of Nov 91)	F_{1400} ($\times 10^{-14}$ ergs cm^{-2} s^{-1} Å^{-1})	$\sigma_{F_{1400}}$	Spectral Index α_{SWP}	$\sigma_{\alpha_{SWP}}$	χ^2_ν
SWP 42969	1.87912	11.6800	0.1616	0.881	0.057	3.917
SWP 42970	1.94888	11.8200	0.1630	0.855	0.057	3.398
SWP 42971	2.01254	12.0900	0.1663	0.777	0.057	3.707
SWP 42972	2.07773	12.0600	0.1657	0.961	0.057	3.713
SWP 42979	2.86603	13.7800	0.1880	0.860	0.053	2.992
SWP 42980	2.93207	14.2300	0.1938	0.740	0.053	4.751
SWP 42995	3.87643	14.0900	0.1918	0.760	0.053	3.718
SWP 42996	3.94092	14.0000	0.1975	0.879	0.064	3.213
SWP 43008	4.86099	15.8900	0.2152	0.771	0.049	3.569
SWP 43009	4.93195	15.9400	0.2153	0.768	0.049	3.775
SWP 43017	5.87164	16.2400	0.2190	0.847	0.049	3.525
SWP 43018	5.94727	16.5800	0.2232	0.736	0.049	3.839
SWP 43025	7.00403	14.9100	0.2016	0.789	0.049	5.203
SWP 43026	7.07547	14.7000	0.1991	0.885	0.049	3.949
SWP 43040	9.19641	18.0200	0.2402	0.734	0.045	3.845
SWP 43041	9.27063	18.5000	0.2476	0.710	0.045	3.327
SWP 43047	9.71866	18.9900	0.2537	0.772	0.045	3.749
SWP 43048	9.77417	18.7100	0.2633	0.887	0.060	3.834
SWP 43054	10.70386	20.7100	0.2749	0.688	0.041	4.008
SWP 43055	10.77008	20.8600	0.2774	0.677	0.045	4.105
SWP 43056	10.83871	20.8500	0.2782	0.759	0.045	3.364
SWP 43057	10.90527	21.1300	0.2810	0.750	0.045	3.783
SWP 43058	10.97137	20.9500	0.2790	0.743	0.045	3.591
SWP 43059	11.03726	21.1200	0.2804	0.722	0.041	4.201
SWP 43060	11.10294	21.2100	0.2840	0.758	0.045	3.133
SWP 43061	11.16980	21.7500	0.2890	0.711	0.041	3.692
SWP 43062	11.23703	22.2600	0.2988	0.753	0.049	3.439
SWP 43063	11.30371	22.1100	0.3033	0.678	0.057	4.099
SWP 43064	11.37048	22.6500	0.3023	0.750	0.045	4.225
SWP 43065	11.83447	22.0900	0.2919	0.727	0.041	4.024
SWP 43066	11.90454	22.3400	0.2974	0.732	0.045	3.853
SWP 43067	11.96689	22.3000	0.2944	0.779	0.041	2.887
SWP 43068	12.03357	23.0000	0.3041	0.722	0.041	4.573
SWP 43069	12.10080	22.3500	0.2957	0.772	0.041	4.018
SWP 43070	12.16840	21.7800	0.2892	0.821	0.045	3.384
SWP 43071	12.23428	21.1200	0.2804	0.809	0.045	3.665
SWP 43073	12.51471	18.8900	0.2947	1.016	0.090	2.946
SWP 43074	12.56787	20.6700	0.2749	0.760	0.045	3.883
SWP 43075	12.63367	20.7800	0.2763	0.776	0.045	4.197
SWP 43076	12.70255	21.0700	0.2808	0.784	0.045	3.841
SWP 43077	12.76688	21.3900	0.2794	0.780	0.038	3.616
SWP 43078	12.83356	21.3100	0.2828	0.797	0.041	3.679
SWP 43079	12.89929	21.8800	0.2903	0.797	0.041	3.138
SWP 43080	12.96588	21.8600	0.2896	0.819	0.041	3.899
SWP 43081	13.03345	21.4900	0.2857	0.860	0.045	4.173
SWP 43082	13.10092	20.9100	0.2788	0.813	0.045	3.697
SWP 43083	13.16806	20.4200	0.2727	0.844	0.045	3.693
SWP 43084	13.23126	19.9700	0.2667	0.764	0.045	4.003
SWP 43085	13.29907	19.6300	0.2641	0.838	0.049	3.666
SWP 43086	13.36594	19.6400	0.2568	0.758	0.038	4.387
SWP 43088	13.50720	19.1800	0.2687	0.942	0.060	3.498
SWP 43089	13.56894	20.0200	0.2708	0.767	0.049	3.651
SWP 43090	13.63153	20.3000	0.2708	0.718	0.045	4.344
SWP 43091	13.69809	20.0100	0.2668	0.833	0.045	4.346
SWP 43092	13.76599	19.6500	0.2625	0.809	0.045	3.698
SWP 43093	13.83084	19.3000	0.2574	0.755	0.045	3.078
SWP 43094	13.89709	18.9600	0.2529	0.740	0.045	3.208
SWP 43095	13.96570	18.3800	0.2467	0.739	0.049	3.861
SWP 43096	14.03030	18.4000	0.2462	0.755	0.045	3.680
SWP 43097	14.09653	18.0600	0.2418	0.779	0.045	3.569
SWP 43098	14.16336	17.9200	0.2399	0.798	0.045	3.755
SWP 43099	14.23135	17.7800	0.2387	0.833	0.049	3.510
SWP 43101	14.56296	18.7000	0.2497	0.770	0.045	4.200
SWP 43102	14.62903	19.0700	0.2543	0.802	0.045	4.055
SWP 43103	14.69815	19.5200	0.2610	0.846	0.045	3.618
SWP 43104	14.76279	19.9900	0.2659	0.854	0.045	3.592
SWP 43105	14.82904	20.4300	0.2717	0.819	0.045	3.717
SWP 43106	14.89505	20.6500	0.2740	0.766	0.041	3.698
SWP 43107	14.96176	20.2500	0.2690	0.816	0.045	3.427
SWP 43108	15.02841	20.4200	0.2711	0.729	0.041	3.590
SWP 43109	15.09451	20.1700	0.2678	0.733	0.041	3.994
SWP 43110	15.16229	19.5300	0.2603	0.786	0.045	3.821
SWP 43111	15.22717	19.7900	0.2633	0.807	0.045	4.813
SWP 43114	16.20871	21.4200	0.2837	0.813	0.041	3.963
SWP 43115	16.26831	21.4600	0.2895	0.832	0.049	4.100
SWP 43121	16.86020	22.1400	0.2929	0.727	0.041	3.614
SWP 43122	16.92563	22.8200	0.3005	0.668	0.041	3.813
SWP 43135	17.86005	21.3700	0.2844	0.778	0.045	3.734
SWP 43136	17.92896	21.3600	0.2828	0.739	0.041	3.600
SWP 43145	18.83432	19.3500	0.2573	0.847	0.045	3.267
SWP 43146	18.90332	18.7700	0.2503	0.920	0.045	4.066
SWP 43157	20.05450	18.6300	0.2483	0.848	0.045	3.303
SWP 43158	20.11401	18.0000	0.2478	0.944	0.057	2.800
SWP 43164	20.71451	20.1300	0.2676	0.867	0.045	3.645
SWP 43165	20.77444	19.4600	0.2728	0.955	0.060	4.011
SWP 43174	21.69171	18.5600	0.2478	0.939	0.045	3.911
SWP 43175	21.76627	18.7400	0.2501	0.932	0.045	3.583
SWP 43184	22.68073	19.4800	0.2598	0.811	0.045	3.747
SWP 43185	22.74625	19.4000	0.2606	0.826	0.049	3.755
SWP 43192	23.70206	21.3400	0.2834	0.816	0.041	4.284
SWP 43193	23.76813	21.0300	0.2825	0.897	0.049	3.511
SWP 43211	24.70337	20.0400	0.2668	0.782	0.045	3.758
SWP 43220	25.69824	19.6400	0.2622	0.819	0.045	3.393
SWP 43221	25.76685	19.6500	0.2636	0.801	0.045	3.576
SWP 43230	26.69736	22.8400	0.3027	0.791	0.041	3.955
SWP 43231	26.76675	23.4000	0.3128	0.842	0.045	3.383
SWP 43236	27.69647	20.9400	0.2781	0.806	0.041	3.942
SWP 43237	27.76450	20.8300	0.2780	0.886	0.045	3.161
SWP 43246	28.87381	21.9100	0.2923	0.909	0.045	4.232
SWP 43247	28.93491	22.1400	0.2949	0.871	0.045	3.695
SWP 43260	29.84335	22.9300	0.3041	0.727	0.041	4.265
SWP 43261	29.90997	22.7000	0.3019	0.832	0.045	4.116

TABLE 2—*Continued*

IUE Image	Observation Midpoint (UT) (Day of Nov 91)	F_{2800} ($\times 10^{-14}$ ergs cm^{-2} s^{-1} Å^{-1})	$\sigma_{F_{2800}}$	Spectral Index α_{LWP}	$\sigma_{\alpha_{LWP}}$	χ^2_ν
LWP 21607	1.84244	4.6230	0.0669	0.697	0.142	1.775
LWP 21608	1.91510	4.7150	0.0682	0.934	0.142	2.376
LWP 21609	1.97968	4.7130	0.0706	0.972	0.161	2.204
LWP 21610	2.04449	4.7990	0.0716	0.938	0.161	2.152
LWP 21611	2.10934	4.8180	0.0713	0.740	0.154	1.949
LWP 21616	2.83383	5.2770	0.0766	0.585	0.146	2.255
LWP 21617	2.89771	5.3020	0.0774	0.927	0.150	2.065
LWP 21625	3.84235	5.2430	0.0762	0.490	0.146	2.397
LWP 21626	3.91318	5.4070	0.0783	0.692	0.142	2.564
LWP 21636	4.82599	6.1480	0.0872	0.985	0.131	2.039
LWP 21637	4.89694	6.1810	0.0880	0.964	0.135	2.373
LWP 21644	5.83676	6.2380	0.0882	0.755	0.127	2.357
LWP 21645	5.91180	6.3510	0.0897	0.735	0.127	2.052
LWP 21652	6.82202	6.1910	0.0876	0.778	0.131	2.385
LWP 21653	7.03946	5.8710	0.0833	0.678	0.131	2.117
LWP 21654	7.11139	5.9320	0.0848	0.879	0.135	2.019
LWP 21667	9.04929	6.9190	0.0968	0.847	0.124	2.400
LWP 21668	9.23254	7.1040	0.0996	1.155	0.124	2.538
LWP 21673	9.68405	7.3060	0.1019	0.854	0.120	2.375
LWP 21674	9.75076	7.3250	0.1022	0.887	0.120	2.521
LWP 21683	10.67126	7.8460	0.1086	0.903	0.116	2.805
LWP 21684	10.73682	7.8530	0.1083	0.751	0.112	1.748
LWP 21685	10.80591	7.9180	0.1095	0.854	0.116	2.285
LWP 21686	10.87241	7.9760	0.1102	0.908	0.112	2.306
LWP 21687	10.93814	7.8680	0.1088	0.653	0.116	1.980
LWP 21688	11.00476	7.9780	0.1101	0.820	0.112	2.488
LWP 21689	11.07086	8.0130	0.1105	0.770	0.112	2.558
LWP 21690	11.13641	8.1230	0.1117	0.723	0.112	2.376
LWP 21691	11.20306	8.3940	0.1164	0.901	0.116	2.414
LWP 21692	11.26898	8.5300	0.1217	0.748	0.135	2.290
LWP 21693	11.33670	8.5630	0.1206	0.693	0.127	2.503
LWP 21696	11.87045	8.5250	0.1169	0.707	0.109	2.732
LWP 21697	11.93353	8.5700	0.1167	0.641	0.105	1.939
LWP 21698	12.00150	8.7160	0.1193	0.772	0.109	2.496
LWP 21699	12.06717	8.7480	0.1187	0.663	0.101	3.072
LWP 21700	12.13443	8.6080	0.1171	0.795	0.105	2.691
LWP 21701	12.20102	8.5050	0.1170	0.968	0.109	2.687
LWP 21702	12.26740	8.2260	0.1127	0.771	0.109	2.509
LWP 21704	12.53397	8.1640	0.1121	0.655	0.109	3.045
LWP 21705	12.60086	8.2070	0.1128	0.875	0.109	2.260
LWP 21706	12.66708	8.1920	0.1128	0.752	0.112	2.374
LWP 21707	12.73361	8.2920	0.1142	0.842	0.112	2.662
LWP 21708	12.79990	8.6660	0.1193	1.241	0.112	4.104
LWP 21709	12.86646	8.3230	0.1144	0.786	0.109	2.425
LWP 21710	12.93216	8.5110	0.1156	0.837	0.101	2.322
LWP 21711	13.00006	8.4760	0.1165	0.957	0.109	2.386
LWP 21712	13.06924	8.2690	0.1138	0.934	0.112	2.498
LWP 21713	13.13214	8.0630	0.1109	0.776	0.112	2.394
LWP 21714	13.19809	7.9180	0.1094	0.897	0.112	2.441
LWP 21715	13.26642	7.6570	0.1071	0.678	0.124	2.438
LWP 21716	13.33105	7.5940	0.1061	0.792	0.120	2.559
LWP 21717	13.53159	7.7690	0.1075	0.882	0.116	2.648
LWP 21718	13.59872	7.8320	0.1080	0.687	0.112	2.260
LWP 21719	13.66470	7.9080	0.1094	0.862	0.116	2.380
LWP 21720	13.73138	7.6380	0.1059	0.768	0.116	2.534
LWP 21721	13.79739	7.6450	0.1057	0.892	0.112	2.570
LWP 21722	13.86356	7.3160	0.1009	0.685	0.112	2.374
LWP 21723	13.93060	7.2740	0.1007	0.896	0.116	2.952
LWP 21724	13.99689	7.1100	0.0983	0.713	0.112	2.379
LWP 21725	14.06299	7.1500	0.0990	0.931	0.116	2.976
LWP 21726	14.12988	7.0930	0.0985	0.921	0.116	2.143
LWP 21727	14.19751	7.0190	0.0979	0.784	0.120	2.156
LWP 21728	14.26501	7.0270	0.0965	0.700	0.109	2.421
LWP 21730	14.52951	7.2790	0.1015	0.889	0.120	2.396
LWP 21731	14.59549	7.5110	0.1039	0.780	0.116	2.830
LWP 21732	14.66269	7.6730	0.1063	0.896	0.116	2.427
LWP 21733	14.72964	7.8020	0.1080	0.830	0.116	2.123
LWP 21734	14.79572	8.0160	0.1096	0.905	0.109	2.764
LWP 21735	14.86139	8.0320	0.1098	0.761	0.109	2.442
LWP 21736	14.92819	7.9950	0.1096	0.914	0.109	2.460
LWP 21737	14.99469	8.0120	0.1099	0.935	0.109	2.581
LWP 21738	15.06076	7.9780	0.1091	0.804	0.109	2.580
LWP 21739	15.12793	7.8050	0.1070	0.774	0.109	2.395
LWP 21740	15.19437	7.7950	0.1072	0.859	0.112	2.462
LWP 21741	15.26242	8.0120	0.1083	0.999	0.097	2.718
LWP 21744	15.82483	7.6290	0.1056	0.883	0.116	2.398
LWP 21747	16.17667	8.3520	0.1147	0.914	0.109	2.562
LWP 21748	16.24106	8.4620	0.1161	0.816	0.109	2.403
LWP 21755	16.82968	8.4450	0.1160	0.768	0.109	2.654
LWP 21756	16.89108	8.7600	0.1199	0.958	0.109	2.106
LWP 21768	17.82776	8.1080	0.1118	0.803	0.112	2.280
LWP 21769	17.89197	8.3060	0.1142	0.766	0.112	1.918
LWP 21777	18.86792	7.8310	0.1076	0.889	0.112	2.308
LWP 21778	18.93918	7.8110	0.1009	0.719	0.064	2.642
LWP 21786	20.02225	7.4050	0.1031	1.067	0.120	2.139
LWP 21787	20.08722	7.4130	0.1020	0.834	0.112	2.238
LWP 21793	20.74850	8.3290	0.1141	0.845	0.109	2.544
LWP 21799	21.72665	7.6930	0.1064	0.947	0.116	1.758
LWP 21810	22.71548	7.9510	0.1094	0.909	0.112	2.110
LWP 21811	22.77560	7.8670	0.1086	0.837	0.116	2.269
LWP 21828	23.73749	8.7470	0.1198	0.914	0.109	2.281
LWP 21837	24.76144	8.0990	0.1099	0.934	0.101	2.703
LWP 21847	25.73145	7.8290	0.1092	0.882	0.120	2.639
LWP 21856	26.73236	9.3260	0.1270	0.841	0.105	2.797
LWP 21864	27.73346	8.4550	0.1157	0.938	0.109	2.219
LWP 21877	28.84067	9.0620	0.1236	0.916	0.105	2.538
LWP 21878	28.90332	9.1780	0.1248	0.920	0.105	2.252
LWP 21888	29.87552	9.2210	0.1256	0.668	0.105	2.619
LWP 21889	29.94113	9.1820	0.1250	0.855	0.105	2.427

TABLE 3

POWER-LAW FITS TO MERGED SWP-LWP SPECTRA

Spectral Pair Image Numbers SWP	LWP	Observation Midpoint (UT) (Day of Nov 91)	F_{2000} ($\times 10^{-14}$ ergs cm^{-2} s^{-1} Å^{-1})	$\sigma_{F_{2000}}$	Spectral Index α_C	σ_{α_C}	χ^2_ν
42969	21607	1.86078	5.9859	0.0779	0.6240	0.0234	0.833
42970	21608	1.93201	6.0642	0.0788	0.6490	0.0234	0.881
42971	21609	1.99609	6.1090	0.0796	0.6200	0.0239	0.819
42972	21610	2.06110	6.2548	0.0816	0.6260	0.0243	1.002
42972	21611	2.09354	6.2716	0.0817	0.6290	0.0237	0.936
42979	21616	2.84991	6.8937	0.0896	0.5780	0.0227	0.831
42980	21617	2.91489	6.9639	0.0902	0.5520	0.0220	1.035
42995	21625	3.85938	6.8988	0.0894	0.5390	0.0218	0.908
42996	21626	3.92706	7.0487	0.0918	0.5830	0.0243	0.923
43008	21636	4.84351	7.9526	0.1027	0.6130	0.0214	0.880
43009	21637	4.91443	8.0223	0.1035	0.6110	0.0207	0.951
43017	21644	5.85419	8.0999	0.1044	0.5800	0.0209	1.901
43018	21645	5.92953	8.2564	0.1066	0.5950	0.0214	0.874
43025	21652	6.91302	7.8411	0.1012	0.7200	0.0214	1.070
43026	21653	7.05746	7.3442	0.0949	0.6300	0.0218	3.953
43026	21654	7.09344	7.6212	0.0984	0.6620	0.0209	0.898
43040	21667	9.12286	8.9753	0.1153	0.6020	0.0191	0.960
43041	21668	9.25159	9.1723	0.1179	0.6140	0.0200	0.988
43047	21673	9.70135	9.4772	0.1219	0.6010	0.0198	0.926
43048	21674	9.76245	9.4906	0.1233	0.6070	0.0234	1.011
43054	21683	10.68756	10.1939	0.1307	0.5880	0.0188	1.089
43055	21684	10.75345	10.2047	0.1309	0.5790	0.0188	0.826
43056	21685	10.82233	10.3228	0.1324	0.5810	0.0186	0.899
43057	21686	10.88885	10.4067	0.1333	0.5740	0.0184	0.975
43058	21687	10.95477	10.2889	0.1320	0.5610	0.0188	0.855
43059	21688	11.02100	10.3994	0.1331	0.5760	0.0184	0.961
43060	21689	11.08691	10.4654	0.1343	0.5690	0.0191	0.903
43061	21690	11.15311	10.6500	0.1365	0.5540	0.0186	0.944
43062	21691	11.22003	10.9667	0.1409	0.5690	0.0195	0.967
43063	21692	11.28635	10.9578	0.1420	0.6220	0.0227	0.904
43064	21693	11.35358	11.1509	0.1431	0.5750	0.0195	0.953
43065	21696	11.85248	11.0276	0.1411	0.6090	0.0181	1.014
43066	21697	11.91904	11.1152	0.1423	0.5960	0.0181	0.849
43067	21698	11.98419	11.2635	0.1441	0.6220	0.0177	0.860
43068	21699	12.05035	11.3657	0.1452	0.5850	0.0175	1.171
43069	21700	12.11761	11.1887	0.1430	0.5980	0.0177	1.057
43070	21701	12.18469	11.0182	0.1411	0.6190	0.0184	1.024
43071	21702	12.25085	10.6448	0.1362	0.6130	0.0179	0.958
43073	21704	12.52435	10.3198	0.1367	0.7240	0.0294	0.928
43074	21705	12.58435	10.5344	0.1350	0.6540	0.0186	0.889
43075	21706	12.65039	10.5557	0.1353	0.6360	0.0186	0.955
43076	21707	12.71811	10.6899	0.1370	0.6350	0.0188	0.996
43077	21708	12.78345	11.0509	0.1414	0.6890	0.0181	1.334
43078	21709	12.85004	10.7665	0.1378	0.6190	0.0181	0.959
43079	21710	12.91574	11.0285	0.1410	0.6100	0.0177	0.903
43080	21711	12.98297	10.9998	0.1406	0.6080	0.0177	1.027
43081	21712	13.05136	10.7693	0.1378	0.5900	0.0181	1.056
43082	21713	13.11655	10.4873	0.1344	0.5960	0.0186	0.963
43083	21714	13.18307	10.2873	0.1320	0.6040	0.0191	0.981
43084	21715	13.24884	9.9549	0.1281	0.5920	0.0195	0.982
43085	21715	13.28275	9.9238	0.1276	0.6100	0.0200	0.950
43086	21716	13.34851	9.8422	0.1261	0.6090	0.0186	1.051
43088	21717	13.51941	9.9996	0.1296	0.6500	0.0227	1.000
43089	21718	13.58383	10.1054	0.1300	0.6240	0.0200	0.883
43090	21719	13.64813	10.1821	0.1307	0.6300	0.0193	1.011
43091	21720	13.71472	10.0029	0.1284	0.5730	0.0193	1.140
43092	21721	13.78168	9.8835	0.1269	0.6160	0.0191	0.948
43093	21722	13.84720	9.5388	0.1223	0.5750	0.0188	0.864
43094	21723	13.91385	9.4330	0.1211	0.6020	0.0191	1.000
43095	21724	13.98129	9.1971	0.1182	0.6110	0.0195	0.940
43096	21725	14.04663	9.2319	0.1185	0.6220	0.0193	1.051
43097	21726	14.11322	9.1581	0.1175	0.6320	0.0193	0.882
43098	21727	14.18042	9.0881	0.1167	0.6220	0.0193	0.917
43099	21728	14.24817	9.0826	0.1166	0.6270	0.0193	0.943
43101	21730	14.54623	9.4185	0.1210	0.6190	0.0198	1.007
43102	21731	14.61224	9.6806	0.1241	0.6330	0.0186	1.001
43103	21732	14.68042	9.9503	0.1278	0.6210	0.0193	0.977
43104	21733	14.74622	10.1550	0.1301	0.6070	0.0186	0.970
43105	21734	14.81238	10.3669	0.1327	0.6250	0.0181	1.074
43106	21735	14.87823	10.3875	0.1329	0.6170	0.0181	0.939
43107	21736	14.94498	10.3210	0.1321	0.6350	0.0181	0.961
43108	21737	15.01154	10.2987	0.1318	0.6410	0.0181	0.946
43109	21738	15.07764	10.2264	0.1310	0.6520	0.0184	0.968
43110	21739	15.14511	10.0141	0.1283	0.6570	0.0186	0.923
43111	21740	15.21075	10.0667	0.1289	0.6320	0.0184	1.118
43111	21741	15.24481	10.2396	0.1309	0.6800	0.0177	1.182
43114	21747	16.19269	10.8351	0.1385	0.6150	0.0179	1.084
43115	21748	16.25470	10.9505	0.1405	0.6240	0.0191	1.024
43121	21755	16.84494	10.9845	0.1406	0.5900	0.0181	0.973
43122	21756	16.90836	11.3194	0.1445	0.6140	0.0175	0.917
43135	21768	17.84390	10.5614	0.1355	0.5770	0.0188	0.913
43136	21769	17.91046	10.7159	0.1372	0.6230	0.0181	0.799
43145	21777	18.85114	10.0257	0.1285	0.6720	0.0184	0.906
43146	21778	18.92126	9.9314	0.1270	0.7020	0.0177	1.028
43157	21786	20.03839	9.5462	0.1227	0.6460	0.0193	0.900
43158	21787	20.10062	9.4811	0.1220	0.6800	0.0209	0.820
43164	21793	20.73151	10.6023	0.1359	0.7040	0.0186	0.940
43165	21793	20.76147	10.5371	0.1364	0.7350	0.0225	0.957
43174	21799	21.70917	9.8364	0.1263	0.6960	0.0193	0.892
43175	21799	21.74646	9.8784	0.1268	0.6800	0.0188	0.919
43184	21810	22.69812	10.1398	0.1300	0.6910	0.0188	0.901
43185	21811	22.76093	10.0724	0.1295	0.6740	0.0198	0.930
43192	21828	23.71979	11.1318	0.1424	0.6990	0.0181	0.981
43193	21828	23.75281	11.1296	0.1428	0.7070	0.0191	0.908
43211	21837	24.73242	10.3553	0.1326	0.6780	0.0181	1.011
43220	21847	25.71484	10.0799	0.1294	0.6490	0.0193	0.981
43221	21847	25.74915	10.0725	0.1295	0.6510	0.0198	0.997
43230	21856	26.71484	11.8615	0.1517	0.6960	0.0177	1.000
43231	21856	26.74957	12.0291	0.1542	0.6430	0.0186	1.029
43236	21864	27.71497	10.8215	0.1387	0.6740	0.0184	0.950
43237	21864	27.74896	10.8460	0.1390	0.6710	0.0186	0.891
43246	21877	28.85724	11.5794	0.1483	0.6940	0.0184	1.022
43247	21878	28.91913	11.6725	0.1494	0.7070	0.0184	0.918
43260	21888	29.85944	11.7367	0.1502	0.6780	0.0181	1.002
43261	21889	29.92554	11.7411	0.1503	0.6730	0.0181	0.998

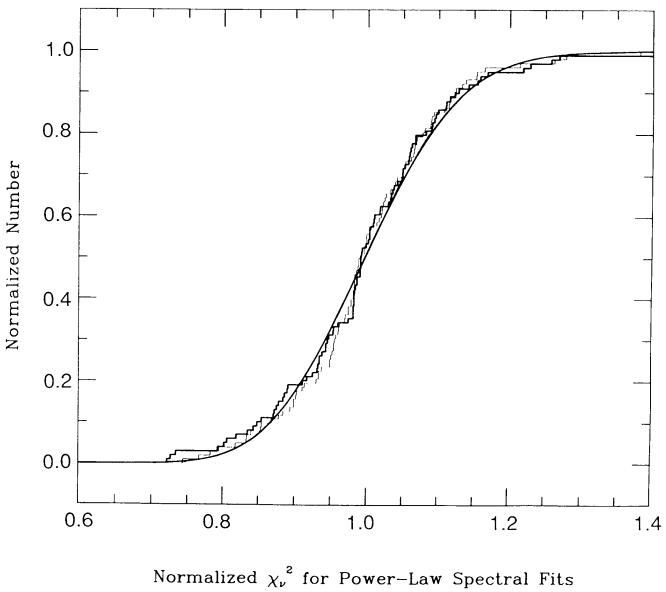

FIG. 2.—Cumulative distribution of normalized reduced χ^2 values for power-law fits to the 99 LWP (*dark histogram*) and 102 SWP spectra (*light histogram*), compared to the expected probability $P(\chi_\nu^2)$ (*curve*). The mean of the distribution is 1, by definition, since the SWET error vector was corrected by the square root of the means of the original distributions ($\langle\chi_\nu^2\rangle = 3.72$ for the SWP and $\langle\chi_\nu^2\rangle = 2.42$ for the LWP). In both cases, a K-S test gives a reasonable probability ($P_{\text{K-S}} > 0.5$) that the observed and expected distributions are the same.

should be distributed as χ^2. (It might be the best approach in the case of a single measurement.) Here we have a large number of measurements (201), so we imposed the condition that the mean of the reduced χ^2 distribution be 1, as is expected for this many degrees of freedom. (The 102 SWP spectra and 99 LWP spectra were handled separately; characteristics of the cameras such as graininess and fixed-pattern noise are quite different, so there is no reason to expect the corrections to the error vectors to be the same in the two cases.)

Scaling the SWET errors by 1.94 for the SWP spectra and 1.56 for the LWP spectra gave normal χ^2 distributions. Not only were the mean values 1, by definition, but a Kolmogorov-Smirnov (K-S) test showed no difference between the observed distributions and the expected $P(\chi_\nu^2)$. (The cumulative χ_ν^2 distributions are shown in Fig. 2.) The uncertainties in the fitted fluxes were thus increased by those factors. A similar procedure was followed for the combined fits, where the mean reduced χ^2 value using the uncorrected sigmas was $\langle\chi_\nu^2\rangle = 3.42$. In this case, however, although the mean of the corrected distribution was adjusted to be 1, a K-S test gave a low probability (4.7×10^{-4}) that the observed distribution was drawn from a normal χ^2 distribution. Thinking this might be related to the different camera characteristics, we refit the combined spectra normalizing SWP errors by 1.94 and LWP errors by 1.56. The resulting reduced χ^2 distribution had a mean of 1.11, so we renormalized the errors by $1.05 = (1.11)^{1/2}$. The final χ_ν^2 distribution, with mean equal to 1, was still incompatible with the expected distribution ($P < 3.9 \times 10^{-5}$ according to a K-S test), probably because of the mismatch between SWP and LWP spectra. This reinforces our belief that the individual fits are better for measuring fluxes or spatial indices, while the combined fits may be more sensitive (due to the broader bandwidth) to trends in either flux or spectral index.

There can still be residual errors in measured quantities, such as spectral index or fiducial fluxes, associated with the reproducibility from one spectrum to the next. These must be included when evaluating light curves. *IUE* fluxes of standard stars are reproducible at the ~1.25% level (Bohlin 1988), so errors of this magnitude were added in quadrature to the internal flux errors estimated above (as in Edelson et al. 1991). In general, the internal photometric error is considerably smaller than 1.25%, unless the exposure time is unusually short. Estimating the repeatability of the spectral index measurements was more complicated. In their study, Clavel et al. (1991) estimated residual errors in measured quantities by comparing close pairs of spectra and assuming no variability on short time scales. If the estimated errors were really 1 σ errors, the difference in measured values divided by the estimated error (the quadrature sum of the two individual error estimates) should be normally distributed, i.e., a Gaussian with zero mean and unit dispersion. A variance larger than one, Clavel et al. argued, meant the uncertainties on that measured quantity should be increased by just that factor. Since PKS 2155-304 is much more rapidly variable than their target, the Seyfert galaxy NGC 5548, this procedure was not appropriate for our flux measurement; hence the 1.25% photometric correction adopted as described above. However, it was the best alternative for evaluating the uncertainty on spectral index, particularly as the spectral index is certainly less variable than the flux (see § 3.2). Adjacent spectra taken closer in time than 5 hr were compared; this included 75 pairs of SWP and 69 pairs of LWP spectra. The variances in the distributions of normalized errors for short- and long-wavelength spectral indices were 1.94 and 2.41, respectively, so the error estimates in α_{SWP} and α_{LWP} were increased by those factors. The distributions of normalized, scaled errors were then consistent ($\gtrsim 50\%$ probability according to a K-S test) with the normal Gaussian distribution expected. This procedure was repeated for combined spectra, comparing 78 pairs of adjacent, combined SWP-LWP spectra, taken within 5 hr of one another. Here, the scale factor for the combined spectral index was 2.18, and the final distribution was consistent with a Gaussian (~59% probability, according to a K-S test).

The estimation of errors in the flux and spectral index, in summary, involves several steps. First, the SWET error vector is propagated through the fitting procedure to get initial uncertainties for the parameters of the power-law fit, b_1 and b_2. Next, uncertainties in both b_1 and b_2 are increased by a factor equal to the square root of the mean of the reduced χ^2 distribution, $\langle\chi_\nu^2\rangle^{1/2}$, where $\langle\chi_\nu^2\rangle = 3.76$ for the SWP and $\langle\chi_\nu^2\rangle = 2.42$ for the LWP. This is effectively scaling up the SWET error vector so that $\langle\chi_\nu^2\rangle = 1$ in both cases. The final error estimate on the flux at λ_0 is equal to the quadrature sum of the scaled error on b_1 and 1.25% of b_1. The final error estimate on the spectral index was derived by increasing the scaled error on b_2 by 1.94 for the SWP, 2.41 for the LWP, and 2.18 for the combined SWP-LWP fits, so that it represents the 1 σ error for the observed differences between adjacent measurements of α. Since this assumes no intrinsic variation between adjacent measurements, it is if anything an overestimate of the error on the spectral index.

As a check, we did look at the distribution of normalized errors in the fluxes, using the uncertainties calculated as described above. In all three cases (SWP, LWP, and combined SWP-LWP values), the distributions were consistent with the expected Gaussian distributions (62%, 13%, and 38% prob-

ability, respectively, according to a K-S test), indicating that our error estimate for the flux is at worst an overestimate.

A procedure similar to that used for determining the uncertainty in spectral indices was used to estimate the global mean uncertainty in the FES-derived magnitude. Using a trial value for the uncertainty, we generated the normalized error distribution for pairs of adjacent measurements separated by less than 5 hr, looking for a value that would give a variance equal to 1. The normalized error distribution for $\Delta V = 0.08$ mag had variance equal to one and was consistent (97% probability according to a K-S test) with a Gaussian distribution centered on zero. It is also commensurate with previous estimates ($\Delta V \sim 0.07$ mag) of the accuracy of the FES (Holm & Crabb 1979; Barylak, Wasatonic, & Imhoff 1984). This is therefore a good estimate of the mean uncertainty in the FES magnitudes, but it does not account for possible infrequent, anomalous FES measurements, for systematic trends in FES errors with FES count rate, or for any systematic offset from other optical measurements (e.g., Smith et al. 1992; Courvoisier et al. 1993), such as might be due to incorrect color corrections.

3. RESULTS

3.1. *Ultraviolet and Optical Light Curves*

The monitoring campaign was a great success. Our BL Lac object cooperated nicely, increasing in intensity by a factor of 2 over the month to roughly its historical maximum brightness. The light curves for the full month and for the central period are shown in Figure 3. During the intensive monitoring, the ultraviolet flux varied by $\sim 30\%$ in several distinct flares that are well sampled apart from a possible dip during the 7 hr gap on November 11. The width of these rapid flares is roughly a half-day; if we define an exponential variability time scale as $t_{\rm var} = (d \ln F/dt)^{-1}$, then values for these flares are less than 2 days. Such fast ultraviolet variations have been detected previously in only two blazars, PKS 2155−304 and Mrk 421, while slightly longer and/or lower amplitude flares have been seen in another three (3C 279, OI 158, and OD 26; Edelson 1992). The ultraviolet flares of PKS 2155−304 show no discernible asymmetry in time according to a dI/I test (Wagner & Witzel 1992). The depth of the dip during November 12 is unclear. The low SWP point comes from a very short exposure of only 13 minutes—most SWP exposures lasted 55 minutes, and the next shortest exposure was 25 minutes—and no corresponding dip is seen in the LWP light curve, so the SWP point should be considered uncertain (see § 3.4).

Based on the rapid flaring seen during the intensive monitoring, it appears we probably failed to sample the fastest time scale flares during the rest of the month, although the overall doubling of the flux is well sampled. The fractional variability is comparable for the SWP and LWP bands: both light curves show a doubling of flux, and in both bands the variance is about 15% of the mean flux. This is in contrast to the historical trends in other blazars, where long-term *IUE* monitoring indicates the SWP flux is more variable than the LWP flux (Edelson 1992).

The FES light curve, shown in Figure 4, shows the same trends as the ultraviolet light curves, on both long and short time scales, although the larger error bars mean the variations are less well defined. Although the light curve is given as V magnitude (from the algorithm used to convert FES counts to optical magnitudes; Perez & Loomis 1991), the FES sensitivity is slightly bluer than the V band.

The SWP, LWP, and FES fluxes are all highly correlated, as shown in the discrete cross-correlation functions (DCF; Edelson & Krolik 1988, with additional minor modifications by J. H. Krolik, unpublished) for SWP versus LWP and SWP versus FES (Fig. 5). The peaks of both DCFs are at zero lag, with an upper limit of $\lesssim 0^d.1$, but both cross-correlation functions are asymmetric, in the sense of the short-wavelength emission leading the longer wavelength emission. These are not necessarily contradictory; see interpretation in § 4.2.

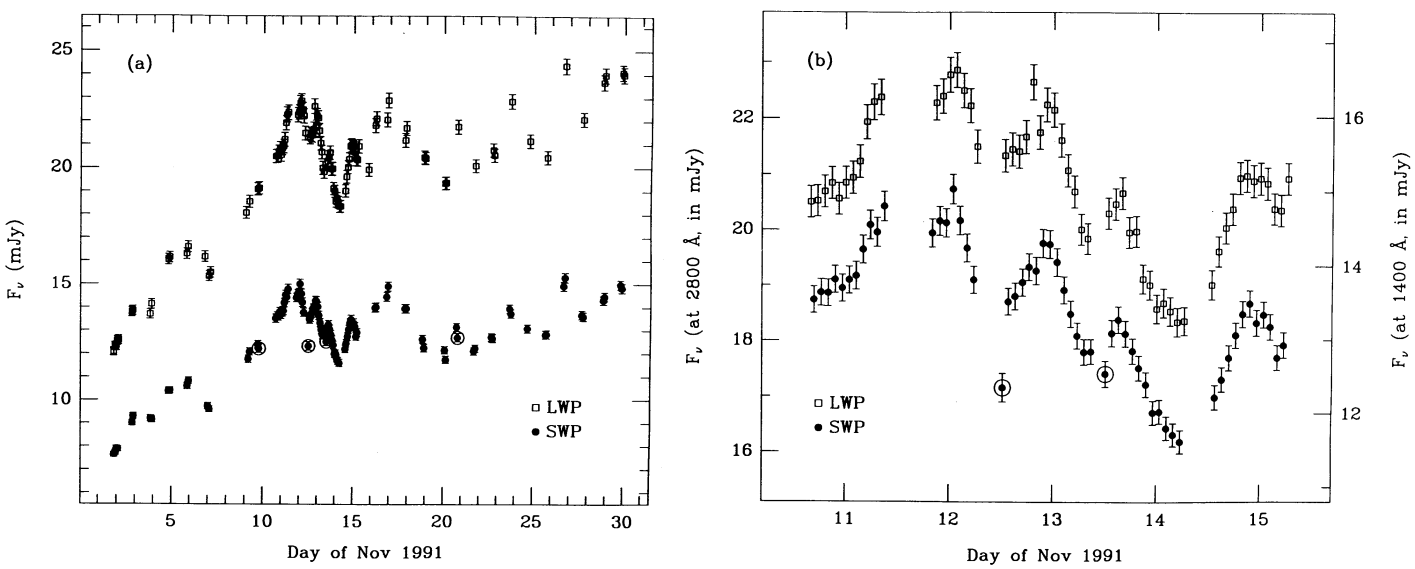

FIG. 3.—Ultraviolet light curves of PKS 2155−304. (*a*) The full month-long light curve, with fitted LWP fluxes at 2800 Å (*open squares*) and SWP fluxes at 1400 Å (*filled circles*) on the same scale. Both long- and short-wavelength fluxes doubled during the month, with no apparent lag. The four SWP fluxes that are uncertain due to anomalously short exposure times are circled. (*b*) Expanded view of the intensive monitoring period, during which *IUE* observations were nearly continuous. The LWP scale is at left; the SWP scale, at right. Many rapid flares have clearly been well sampled. Five cycles with period $\sim 0^d.7$ can be seen, but the reality of the quasi periodicity cannot be established without a longer data train.

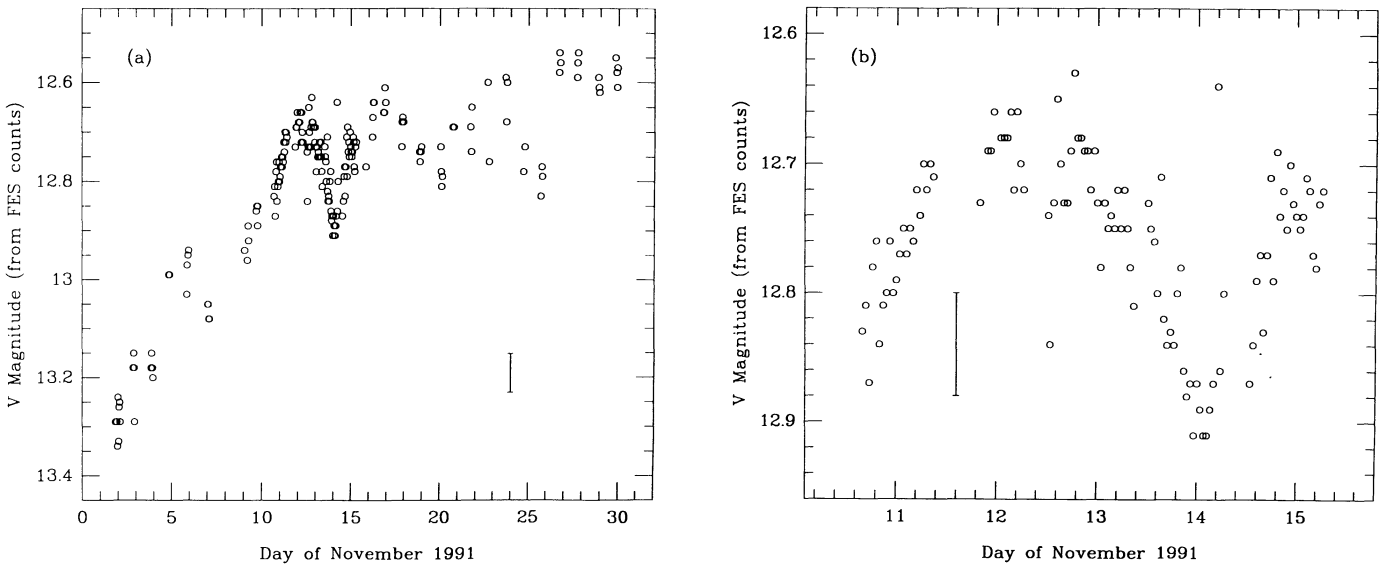

FIG. 4.—Optical light curves deduced from the *IUE* FES monitor for (*a*) the full month and (*b*) the intensive monitoring period. FES counts were converted to approximate *V* magnitude according to the prescription of Perez & Loomis (1991), which takes into account the contribution of scattered light. Typical error bars of ~0.08 mag (see § 2.5) are shown in each panel.

The autocorrelation functions of the SWP, LWP, and FES light curves are shown in Figure 6. The SWP and LWP give similar results, while the FES amplitude is generally smaller because the relative errors are larger. (For the SWP and LWP, the behavior of the autocorrelation functions suggests the estimates of flux errors were about right. Note that in the method of Edelson & Krolik 1988, the amplitude of the cross-correlation or autocorrelation function depends on the binning, and hence the error bars, so that it can be formally larger than unity.) On long time scales, the autocorrelation functions suggest smooth "red" power spectra, with relatively more power on longer time scales. However, on shorter time scales (using the data from the well-sampled, 4.6 day intensive monitoring) they are modulated with a period of $\sim 0^d.7$, with the first harmonic also seen, at $\sim 1^d.5$. This quasi-periodic behavior can be seen going through five cycles in the light curves (Fig. 3*b*), despite the gap at November 11.5.

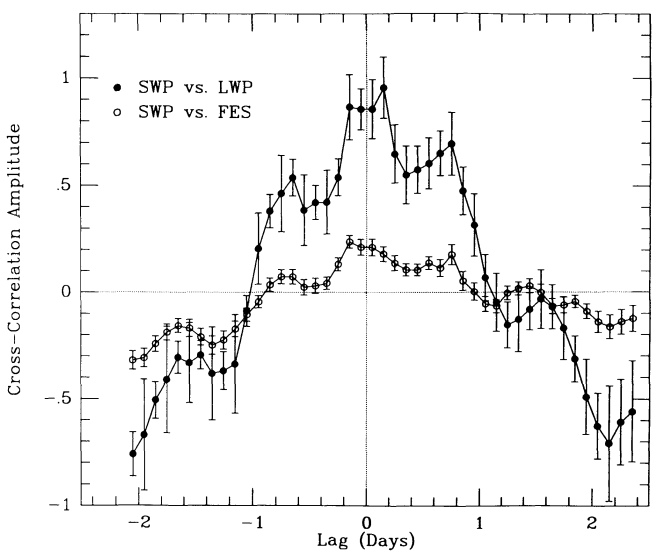

FIG. 5.—Discrete cross-correlations between SWP flux and longer wavelength flux for the intensive monitoring period. *Filled circles:* SWP flux at 1400 Å vs. LWP flux at 2800 Å; *open circles:* SWP vs. FES flux. The light curves are highly correlated, with peak at zero lag (with an upper limit of less than a few hours), and at the same time asymmetric (the excess positive correlation at positive lags corresponds to the short-wavelength emission leading longer wavelength emission).

The significance of this possible periodicity is unclear. Were there only a few peaks ($\lesssim 3$), it could almost certainly be dismissed as spurious (Press 1978). Signals with red power spectra frequently show spurious periodicities on time scales that are an appreciable fraction of the length of the data stream because there are too few large-amplitude components at low frequencies to achieve the Gaussian behavior of the central limit theorem. The fact that the apparent period is closer to one-fifth of the intensively sampled stream, and that the light curve shows little power at other frequencies, tempts us to believe that it may be real; but this would only be a comfortable conclusion if there were 10 or 20 periods (so that the central limit theorem would indeed apply). The sampling in contemporaneous optical monitoring was not sufficient to detect periods shorter than a few days (Smith et al. 1992). This period is not present in extensive, well-sampled optical data taken in 1988 (Carini & Miller 1992), which means, since we now know the optical and ultraviolet are closely related, that any periodicity, if real, is transitory. Only a longer run of intensive monitoring can clearly confirm or refute the stability of this periodicity.

3.2. *Ultraviolet Spectral Variability*

A key point in the interpretation of the continuum emission from PKS 2155−304 is the relationship between variability in intensity and spectral shape. Previous monitoring has suggested that the spectral index varies little during flares in intensity, but this observation was always restricted to grossly undersampled light curves. The present campaign, with its improved sampling, should be more sensitive to related variations in flux and spectral index. The variation of spectral index throughout the run is shown in Figure 7. According to the χ^2 statistic, the model of constant spectral shape can be ruled out:

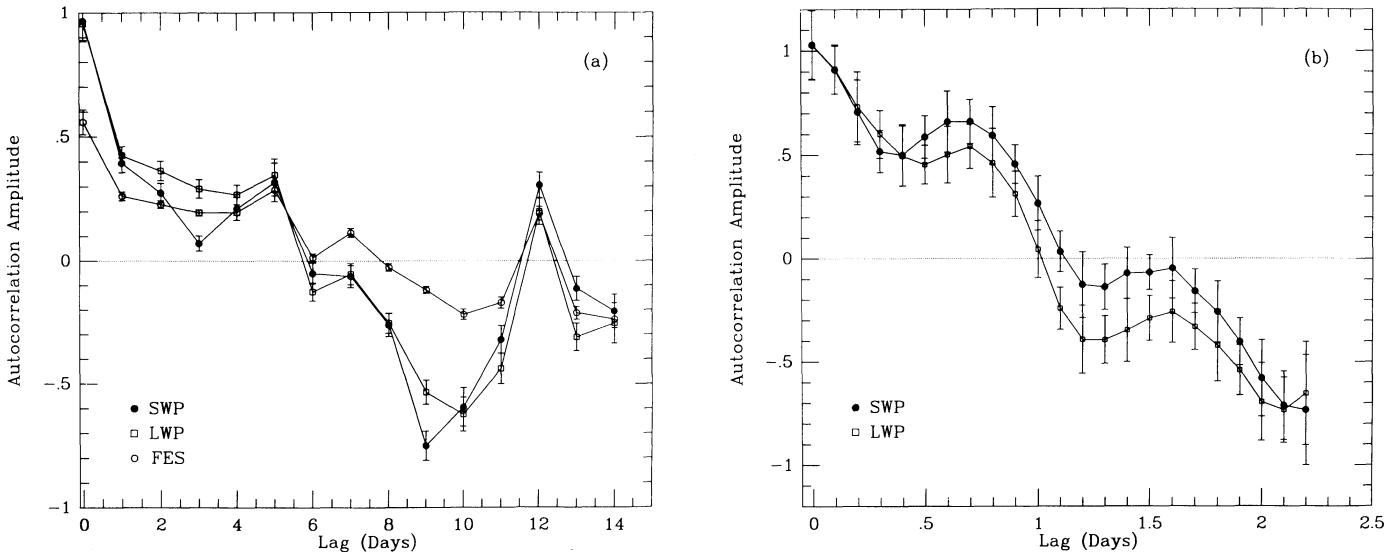

FIG. 6.—Discrete autocorrelation functions for SWP flux at 1400 Å (*filled circles*), LWP flux at 2800 Å (*open squares*), and FES flux (*open circles*). (*a*) Calculated for the full 30 day data set, which is probably undersampled. There is correlation out to several (~5) days. The amplitude of the FES autocorrelation is low because of the larger relative errors in the photometry. (*b*) Calculated for the $4^d.6$ intensive monitoring period only. The SWP and LWP autocorrelation functions are very similar, and both show a peak at a lag of about $0^d.7$.

$\chi_\nu^2 = 4.68$ for the combined spectral index. This is also seen in the SWP camera alone, where $\chi_\nu^2 = 1.94$ [$P(\chi_\nu^2) = 5.9 \times 10^{-8}$] for a constant fit to α_{SWP}. (The variation in the LWP spectral index is not significant, $\chi_\nu^2 = 0.98$, because of the larger errors due to the low signal-to-noise ratio below 2400 Å.)

Plausible physical processes causing intensity variability, such as acceleration of radiating particles near a shock, predict accompanying changes in the spectrum of the emitted radiation. For example, electron acceleration would cause spectral hardening with increasing intensity. Thus one might expect flux and spectral index to be inversely correlated. Such correlations have been found previously for Mrk 421 (Ulrich et al. 1984) and OJ 287 (Maraschi et al. 1986), although these studies referred to data taken over much longer time intervals. In the present case, a nonparametric Spearman rank-order correlation test suggests an inverse correlation between F_{1400} and α_{SWP} ($P = 9.2 \times 10^{-3}$ of occurring by chance for the full data set; $P = 0.07$ for the intensive monitoring period only), but not between F_{2800} and α_{LWP} ($P = 0.87$ and $P = 0.76$ for full and intensive periods, respectively) or F_{2000} and α_C ($P = 0.41$ and $P = 0.19$ for full and intensive periods, respectively). Figure 8*a* shows the scatter plot of the last of these, with filled circles indicating data from the intensive monitoring period.

Previous authors found no correlation between flux and spectral index for PKS 2155−304, but did find a correlation between ΔF and $\Delta\alpha$, where the change is measured between pairs of spectra taken close in time (Maraschi et al. 1986; Urry et al. 1988; Edelson 1992). In the present instance, in contrast,

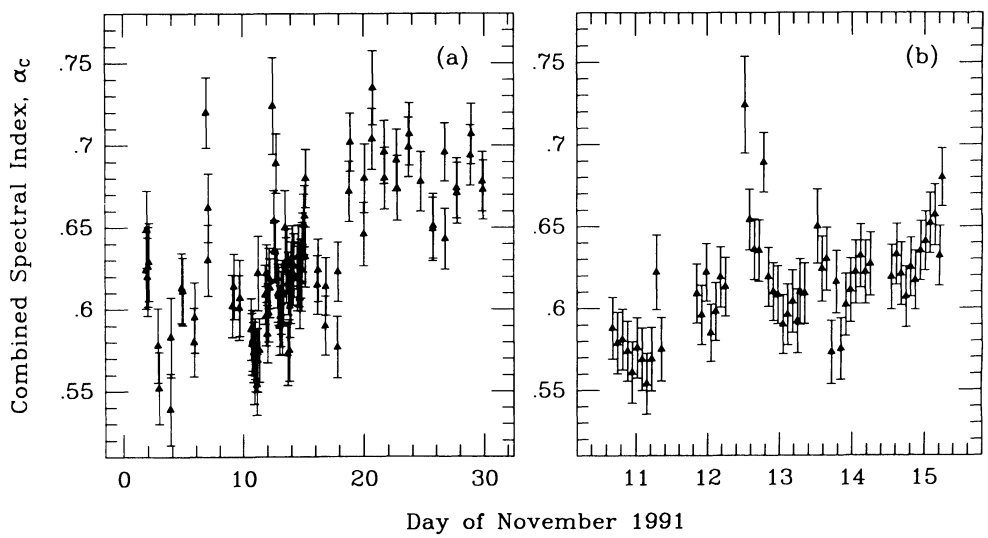

FIG. 7.—Variability of the combined spectral index (*a*) over the full month and (*b*) during the intensive monitoring period. The model of a constant spectral shape has $\chi_\nu^2 = 4.7$, so is strongly rejected.

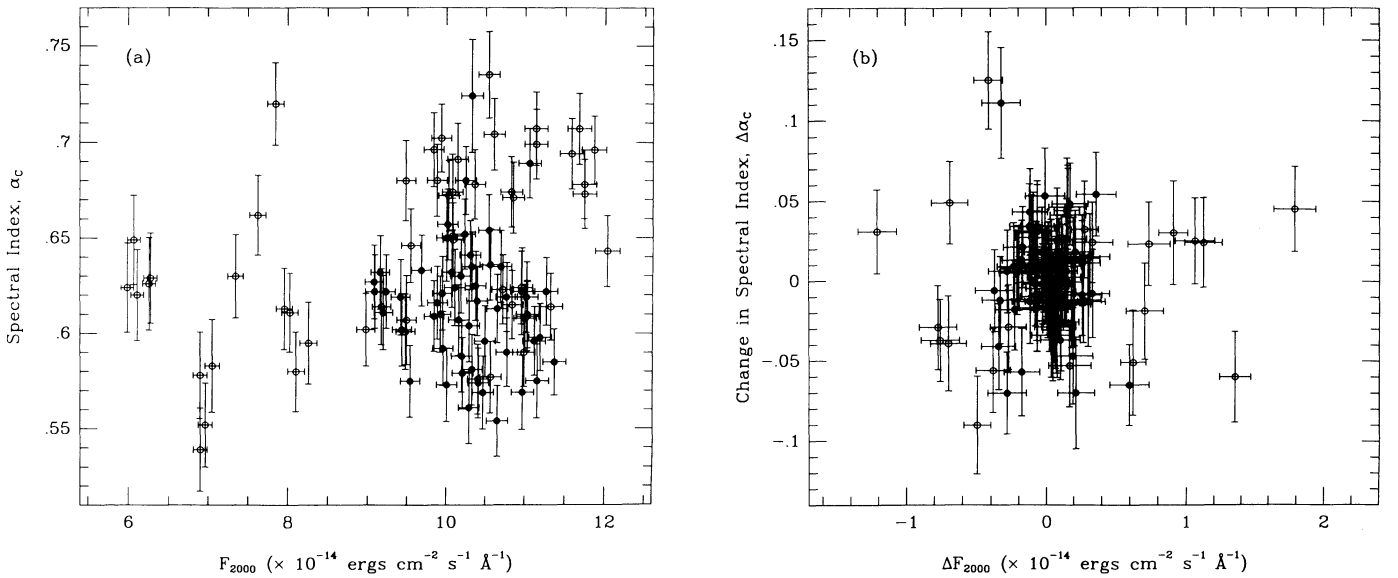

FIG. 8.—Ultraviolet flux vs. spectral index. (*a*) F_{2000} vs. α_C for the full month (*open circles*) and for the intensive monitoring period (*filled circles*). (*b*) ΔF_{2000} vs. $\Delta\alpha_C$ for the full month (*open circles*) and for the intensive monitoring period (*filled circles*). There are no significant correlations according to a Spearman rank-order test.

change in spectral index and change in flux are not strongly correlated; Figure 8*b* shows the change in spectral index versus the change in flux for the combined SWP-LWP spectral fits. The probability of correlation between $\Delta\alpha$ and ΔF for the intensive monitoring period (measured from adjacent data points) is significant only for the lower quality LWP data ($P > 99.9\%$). For the full data stream, using the differences between daily averages, $\Delta\alpha$ and ΔF are marginally anticorrelated for the SWP data (~96.7%). In neither case are the combined SWP-LWP data correlated or anticorrelated. We conclude that there is no significant direct correlation between instantaneous spectral shape and intensity, or changes thereof, in the *IUE* data.

Given the importance of understanding spectral variability, we explored a new tool for measuring the phenomenon. We applied the discrete correlation function (Edelson & Krolik 1988), usually used to investigate flux-flux correlations, to the cross-correlation between flux and spectral index for the intensive monitoring period, where the light curve is well sampled. The results are shown in Figure 9 for the SWP and LWP fits (which track each other well). There is clearly structure in this DCF. The negative lag means that changes in the spectral index precede changes in the intensity, and the negative correlation amplitude means that spectral hardening (decreasing α) is associated with increasing intensity. Thus, there appears to be some kind of inverse correlation between spectral index and intensity, but with a lag of 1–2 days.

3.3. *Ultraviolet Spectral Shape*

The spectral shape in the ultraviolet band depends critically on the dereddening correction. When no correction is applied, the LWP spectral indices are systematically higher than the SWP spectral indices (e.g., Edelson 1992). This implies flattening of the spectrum toward shorter wavelengths; that is, a "concave-up" shape in ν-F_ν space, in contrast to the overall "concave-down" shape of the radio through soft X-ray spectrum. An excess at long wavelengths due to inclusion of starlight is not expected, as the host galaxy for PKS 2155−304 detected in deep optical imaging (Falomo et al. 1991) is too faint ($V \sim 16.5$) relative to the nuclear point source. The spectral curvature goes away, however, when a dereddening correction with $E(B-V) = 0.034$ mag is applied. (If we fit the entire ensemble of combined SWP-LWP spectra to a power-law model leaving the reddening correction as a free parameter, χ^2 is minimized for this value.) Figure 10 shows the distributions of SWP and LWP spectral indices for three assumed values of $E(B-V)$: 0.0 mag, 0.034 mag, and 0.05 mag. With no correc-

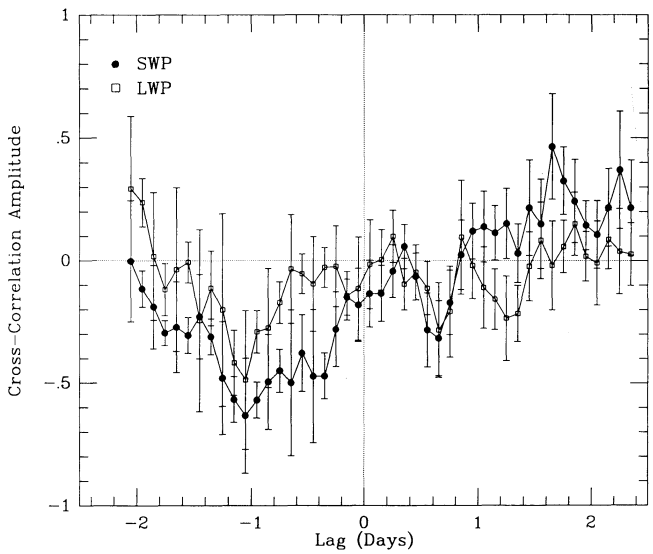

FIG. 9.—Discrete cross-correlation of spectral index vs. intensity for the intensive monitoring period. *Filled circles:* F_{1400} vs. α_{SWP}; *open squares:* F_{2800} vs. α_{LWP}. Note the dip at −1 day. The negative lag means change in the spectral index precedes change in intensity, and the negative correlation amplitude means that spectral hardening (decreasing α) is associated with increasing intensity.

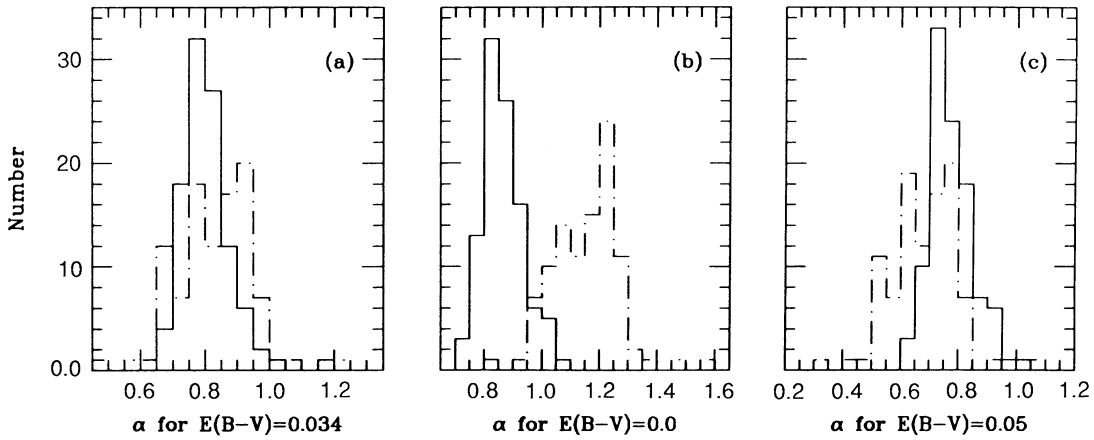

FIG. 10.—Histograms of spectral index distributions for SWP (*solid line*) and LWP (*dot-dash line*). (*a*) Fits presented in Table 2, corrected for reddening using $E(B-V) = 0.034$ mag; (*b*) raw data, not corrected for reddening; (*c*) fits after correction with $E(B-V) = 0.05$ mag. Given the reddening uncertainty, no spectral curvature can be claimed. The reddening correction adopted (panel *a*) brings the SWP and LWP distributions most closely into agreement.

tion, the LWP spectra are steeper; with $E(B-V) = 0.05$ mag, the SWP spectra are steeper; and $E(B-V) = 0.034$ mag is roughly the value at which the SWP and LWP spectral indices agree best. Thus, while the amount of reddening remains uncertain (see § 2.3), the assumption that the ultraviolet spectrum is either a flat power law or concave-down would indicate a minimum reddening of $E(B-V) \sim 0.03$ mag.

Taking the reddening into account, then, there is no evidence for spectral curvature in the ultraviolet band. The flatness of the UV spectral index ($\alpha < 1$) means that peak of the luminosity emitted from this BL Lac object is in the far-ultraviolet, as noted by previous authors.

3.4. *Systematic Errors*

The absolute calibrations and sensitivity corrections are the largest sources of uncertainty in the absolute value of the flux. The *IUE* calibrations available—the one used in our pipeline (Bohlin et al. 1990), the white dwarf calibration being used for the *IUE* Final Archive (Finley et al. 1993), and the standard IUESIPS calibration (Cassatella, Lloyd, & Riestra 1988)—result in calibrated fluxes that differ by less than 10%. The Bohlin calibration tends to be lower than the IUESIPS calibration for the SWP (the average ratio is 0.93).

The SWP sensitivity correction is roughly 1% per year averaged over the whole waveband. The extrapolation from 1988 is uncertain. We have applied no sensitivity correction to the LWP, although one has been published (Teays & Garhart 1990). Such a correction would possibly alleviate the camera mismatch, as in our results the SWP flux is too high relative to the LWP.

There are small systematic differences in the shapes of *IUE* spectra extracted with GEX and with SWET. However, the ratio of the extracted spectra averaged over the full waveband is close to 1. The parameters of the fitted spectral indices in the two wavebands differ systematically (by $\Delta\alpha \sim 0.1$ for the LWP and $\Delta\alpha \sim 0.2$ for the SWP) but the results of combined fits are essentially identical. Therefore, the results are independent of extraction method. (The advantage of the SWET technique, providing independent error estimates for each data point, remains.)

As mentioned earlier, the amount of reddening along the line-of-sight to PKS 2155−304 is uncertain. With no dereddening, the absolute ultraviolet flux would be ~20%–30% lower than the numbers quoted in Table 2 and the spectral shape would be concave-up (i.e., there would be excess long-wavelength flux above the SWP power law). There is no obvious explanation for an intrinsic spectrum of this shape, whereas concave-down spectra can result naturally from synchrotron losses. The available evidence is generally consistent with our assumed value of $E(B-V) = 0.034$ mag, which would correspond to an approximately flat (i.e., not concave-down or -up) spectrum, but the uncertainties are large. One might reduce the uncertainty in $N_{\rm H\,I}$ due to small-scale fluctuations in the interstellar medium by using PKS 2155−304 as a background radio source at 21 cm, although that would introduce another uncertainty due to the unknown spin temperature of the gas. Another approach would be to estimate the extinction in the extreme ultraviolet, which is very sensitive to the H I and He I column densities (particularly the latter), using the recently obtained *EUVE* spectrum (Malina & Bowyer 1992). The total optical depth at 100 eV corresponding to $N_{\rm H\,I} = 1.78 \times 10^{20}$ atoms cm^{-2}, assuming He I is 10% by number, is $\tau \sim 11$, quite high considering that PKS 2155−304 is one of the two brightest extragalactic sources detected with the *ROSAT* WFC (Pounds et al. 1992) and was also detected in the short-wavelength ($E \sim 100$ eV) filter of *EUVE* (Malina & Bowyer).

After our analysis was completed, we learned of an unpublished 21 cm emission measurement by Lockman & Savage (1993), $N_{\rm HI} = 1.36 \times 10^{20}$ cm^{-2}, made with a 21′ beam and careful attention to the antenna sensitivity pattern (e.g., see description in Lockman, Jahoda, & McCammon 1986). This value for the Galactic hydrogen column density, which is somewhat lower than the Stark et al. (1992) value we used, would corresponds to $E(B-V) = 0.026$ mag and would result in lower absolute fluxes than those given in Table 2, by about 6% for the SWP and 3% for the LWP, or about 22% and 18% higher, respectively, than the observed fluxes. The total optical depth at 100 eV for this column density would be $\tau \sim 9$.

In any case, the uncertainty in the gas-to-dust ratio dominates the uncertainties in the assumed $E(B-V)$. The scatter in the conversion factor deduced by Shull & Van Steenberg (1985), for example, gives a 1 σ range for $E(B-V)$ of 0.014 − 0.047 mag. In addition, we used the conversion appropriate to the full sample of 205 stars; a conversion for the 53 halo stars only, $\log N_{\rm H\,I}/E(B-V) = 21.83$ cm^{-2} mag^{-1}, gives

$E(B-V) = 0.026$ mag for the Stark et al. (1992) value of $N_{\rm H\,I}$, or 0.020 mag for the Lockman & Savage value of $N_{\rm H\,I}$, with somewhat larger uncertainties.

Collectively, the uncertainties in absolute calibration, sensitivity corrections, and dereddening corrections amount to 10%–15% uncertainties in the measured absolute flux. However, since the same corrections are applied to all the spectra, the relative fluxes are not affected by these uncertainties.

Like many blazars, PKS 2155−304 can be highly polarized (e.g., Smith et al. 1992; Allen et al. 1993). Because the *IUE* spectrographs use gratings, spurious variability could in principle be introduced by changes in polarization. During the monitoring campaign, the *U*-band polarization of PKS 2155−304 was always $\lesssim 8\%$ (Smith et al. 1992), so that the effect would have been no larger than the quoted uncertainties.

Finally, systematic errors arising in only a handful of spectra or FES images are not taken into account by our error analysis procedure, which assumes that the exposures have similar properties. This is probably a reasonable assumption for most of the data, which were obtained under similar conditions. Exceptions include the four unusually short SWP exposures (points circled in Fig. 3), since short *IUE* exposures have been shown to give systematically low fluxes (Walter & Courvoisier 1991). The errors on quantities measured from these SWP exposures are almost certainly underestimated.

4. DISCUSSION

4.1. *Intensity Variability*

Throughout our month-long observing campaign, the ultraviolet and optical flux of PKS 2155−304 increased by a factor of 2. The light curves are far from smooth, however, with rapid lower amplitude events superposed. During the intensive monitoring period in the middle of the month, there are a number of well-sampled, large-amplitude ($\sim 30\%$) variations which appear to have a quasi-periodic time scale of $\sim 0\overset{d}{.}7$. Whether this periodicity is real requires a longer data train with equal or better sampling. The exponential time scales associated with the most rapid events are a few days or less; the actual time in which flux was seen to double was approximately 10 days. Similar fast, intraday variability, including the appearance of quasi periodicity, has been seen in optical observations of BL Lac objects (Quirrenbach et al. 1991). Such short time scales are consistent with the predictions of the standard relativistic jet and accretion disk models for BL Lac objects (e.g., Königl 1981; Wandel & Urry 1991).

The possible periodicity at ~ 15–20 hr is one of the most intriguing yet ultimately frustrating results of the present campaign. We have sufficient data that we cannot automatically dismiss it as an artifact of the length of observation or of poor sampling; on the other hand, we lack enough data to be confident of its reality. During our observations, PKS 2155−304 was in a particularly bright state, as was the BL Lac object OJ 287 when a possible periodicity was detected in its optical light curve (Carrasco, Dultzin-Hacyan, & Cruz-Gonzalez 1985). It is clearly important to obtain longer, high-quality light curves of PKS 2155−304 in a bright state.

Meanwhile, keeping in mind the uncertainties, we explored what such a period, if real, might mean. One possible origin of a periodicity is orbital motion. The nearest stable orbit around a black hole is at a few ($n \gtrsim 3$) Schwarzschild radii, where $R_{\rm S} = 2GM_{\rm BH}/c^2$. Using Kepler's law and ignoring relativistic effects, the central black hole mass is related to is the orbital period, T, by $M_{\rm BH} = Tc^3/[4(2)^{1/2}\pi n^{3/2}G]$. If the ultraviolet emission is not relativistically beamed, then $M_{\rm BH} < 1.3 \times 10^8\ M_\odot$. Relativistic beaming would shorten the observed time scale relative to the true time scale, and so would allow higher masses in this simple limit.

In the context of a relativistic jet picture, the periodicity can be explained if the production of the jet is closely coupled to the orbital dynamics. For example, Camenzind & Krockenberger (1992) considered jets that are magnetically collimated winds emanating from the inner edge of an accretion disk. In this model, spiraling motion of plasma bubbles moving along magnetic field lines in the jet causes quasi-periodic fluctuations in observed intensity simply as a result of a smooth variation in the Doppler factor. The rotation period of the escaping plasma bubbles is initially the Keplerian period of the inner disk, increasing beyond the Alfvén point, $R_{\rm A}$, as $(R/R_{\rm A})^2$, where R is the perpendicular distance of the bubble from the jet axis. The bubbles become collimated and are observed at $R > R_{\rm A}$. The observed period will be shorter by the factor $(1 - \beta \cos\theta)$, where θ is the inclination of the jet, due to a relativistic projection effect.

For PKS 2155−304 there are no firm estimates of either the Lorentz factor or the inclination angle (cf. Urry & Mushotzky 1982 and Ghisellini et al. 1985), but assuming $\gamma \sim 5$, as appropriate for one of the more active X-ray–selected BL Lac objects (Padovani & Urry 1990), and $\theta \lesssim 1/\gamma \sim 10°$, the observed period of $0\overset{d}{.}7$ corresponds to a true period of 1.7×10^6 s. For $R/R_{\rm A} \sim 10$ (Camenzind & Krockenberger 1992), the Keplerian period at $5R_{\rm S}$ is then 1.7×10^4 s and the black hole mass is $1.8 \times 10^7\ M_\odot$.

The ultraviolet flux from PKS 2155−304 varies between 1.3 and 2.7 and 10^{-10} ergs cm^{-2} s^{-1} (1200–3000 Å). For a redshift of $z \sim 0.12$ (assuming $H_0 = 50$ km s^{-1} Mpc^{-1}, and isotropic emission), this corresponds to an ultraviolet luminosity of 0.9 to 1.9×10^{46} ergs s^{-1}. A 30% change in intensity occurring over a day (for example, around 1991 November 13–14) corresponds to $\Delta L/\Delta t \sim 5 \times 10^{40}$ ergs s^{-2}, which is only a factor of 4 below the fiducial limit for Eddington-limited accretion with efficiency $\eta = 0.1$ (§ 1). We estimate a bolometric correction of ~ 10 for PKS 2155−304 using published multiwavelength data. (Given the flat ultraviolet spectral index, $\alpha < 1$, the bolometric correction depends most strongly on the detailed ultraviolet through soft X-ray spectrum, for which we use the data summarized by Wandel & Urry 1991.) If the UV, extreme UV, and X-ray flux all vary comparably (see Edelson et al. 1993), the flaring monitored in 1991 November would in fact have exceeded the limit, suggesting relativistic beaming is present.

4.2. *Spectral Variability*

The spectral variability observed is intriguing, and not easily interpreted. The fluxes within both *IUE* bands and the optical flux deduced from the FES are all well correlated with no discernible lags on time scales $\gtrsim 3$ hr. The cross-correlation functions are asymmetric, however, in the sense that short-wavelength emission leads the long. This may indicate that the emitting volumes are not significantly different across the ultraviolet band, but that radiative losses are sufficiently energy dependent that the short-wavelength flux decays faster than the long-wavelength flux.

The overall amplitude of variability is roughly the same in the short- and long-wavelength *IUE* bands, but the ultraviolet spectral shape does vary significantly during the campaign. Comparing Figures 3 and 7, we can see that the relation

between intensity and spectral shape is not simple. While the source flux doubled in the first 10 days, the spectral index increased briefly and then returned to roughly its initial level. In the latter half of the month, while the source intensity remained high, the spectral index steepened. During the intensive monitoring period, the flux–spectral index relationship is similarly complicated.

Spectral variability is a strong diagnostic of any emission process. The general sense of the variation in PKS 2155−304 is that the spectrum hardens with increasing intensity, as expected for nonthermal processes where increases (decreases) result from acceleration (radiative losses) of the nonthermal electron population. The apparent temporal lag (~1 day) between change in spectral shape and change in intensity (Fig. 9) is more difficult to interpret.

The specific accretion disk model proposed by Wandel & Urry (1991), which was constructed to fit the ultraviolet spectral shape and estimated ultraviolet variability time scales of PKS 2155−304, is ruled out by the close correlation between optical and ultraviolet *IUE* light curves, since in that model a large fraction of the optical flux had to be produced independently of the ultraviolet flux. Additional arguments against the disk model for PKS 2155−304 are based on the observed wavelength-dependent optical polarization (increasing to the blue; Smith & Sitko 1991; Aitken et al. 1993) and the extremely rapid changes in polarization (Smith et al. 1992).

In contrast, the ultraviolet variability is consistent with what is expected from a relativistic jet. Specifically, Celotti, Maraschi, & Treves (1991) consider the variability characteristics of a range of jet models, assuming that an increase in emissivity is triggered by a signal traveling along the jet, without affecting the local particle spectra. In this case it is possible to produce ultraviolet variability with very small spectral changes. All the models predict much stronger X-ray variability; both the relative amplitude and the lag, if any, are strong constraints on the details of the model. No detailed calculations were attempted here because the associated X-ray variability is the strongest constraint; for further discussion, see Edelson et al. (1993).

The variability could also be caused by gravitational microlensing. Ostriker & Vietri (1985, 1989) have argued that the redshift distribution of BL Lacertae objects can be explained by incorrect identification of the lensing galaxies as the host galaxies of the BL Lac objects, with the true background objects being OVV quasars. Specific candidates for microlensing have been suggested for some of the radio-selected BL Lac objects on the basis of their variability characteristics (Stickel et al. 1991). If the size of the emitting region is independent of wavelength, the variability will be achromatic, as is approximately the case with the *IUE* data for PKS 2155−304. Rapid variations ($t_{\rm var} \ll 1$ yr) through microlensing are possible but require the relative source/lens velocities to be extremely high, such as the superluminal motion that results from an aligned relativistic jet. Calculations of the amplification pattern due to microlensing that include the macrolensing shear can even produce a quasi-periodic signal (Wambsganss, Paczyński, & Katz 1990). Minor spectral changes could be explained by intrinsic effects in the jet, while the bulk of the flux variations could be due to microlensing.

5. CONCLUSIONS

In 1991 November, a large multiwavelength campaign was devoted to monitoring the UV-bright BL Lac object PKS 2155−304, with coverage from radio through X-ray wavelengths. Ultraviolet and optical observations were made with the *IUE* satellite on a daily basis throughout the month. Quasi-continuous coverage, with ~96 minute time resolution, was undertaken during a $4^{d}.6$ period in the middle of the month. The latter data are well sampled, in the sense that the fastest flares, with time scales $\sim 1^{d}$, were clearly resolved.

The month-long observations show a doubling of the flux in about 10^{d}, with smaller, more rapid flares superposed on this general trend. The well-resolved flares during the intensive monitoring have an apparent quasi periodicity of $\sim 0^{d}.7$, although the data train was too short to confirm the reality of the period. Such flares might be expected from disturbances propagating along the magnetic field lines in a jet (Camenzind & Krockenberger 1992).

The large amplitude and short time scale of the fastest observed variability probably requires relativistic beaming (depending on whether emission at other wavelengths varies comparably, so that the bolometric correction of 10 is applicable). In the absence of relativistic effects, however, a simple estimate identifying the periodicity with a Keplerian orbit at the smallest stable orbit around a central black hole limits the black hole mass to $\lesssim 1.3 \times 10^{8}\, M_{\odot}$.

The short- and long-wavelength ultraviolet light curves are well correlated with each other, and with the optical light curve deduced from the Fine Error Sensor (FES) on *IUE*. The formal lag is zero, but the cross-correlation is asymmetric in the sense that shorter wavelength emission leads the longer, suggesting that the loss time scales are faster for the shorter wavelength emission, as expected in the synchrotron process.

Small but significant spectral variability is detected. The ultraviolet spectral index and intensity are inversely correlated (harder spectra corresponding to higher intensity), but the change in index leads the change in intensity by 1 or 2 days. The inverse correlation between spectral index and intensity is consistent with the nonthermal acceleration processes expected in relativistic plasmas, so that the present results are again consistent with relativistic jet models.

The accretion disk scenario of Wandel & Urry (1991) is ruled out by the similarity of the optical and ultraviolet light curves. The general character of the variability is consistent with the expectations of relativistic jet models (Celotti et al. 1991; Camenzind & Krockenberger 1992), and we cannot rule out the importance of gravitational microlensing.

We are grateful to the *IUE* project for important contributions to the observations, particularly Bruce McCollum (Goddard) and Richard Monier (Vilspa), who were in charge of scheduling the observations; the Goddard Telescope Operators (Jim Caplinger, Andy Groebner, Charlie Loomis, Scott Snell, Tom Walker, and Daryl Weinstein) and Resident Astronomers (Richard Arquilla, Michael Carini, Martin England, Cathy Mansperger, Jeff Newmark, Mario Perez, and Lloyd Rawley); and the Vilspa staff (Domitilla de Martino, John Fernley, Rosario Gonzalez, and Antonio Talavera). The IUE Regional Data Analysis Facility was instrumental in making prompt access to the data possible, and Lyla Taylor helpfully provided a replacement tape when one of our original data tapes was unreadable. The Vilspa staff were also extremely helpful in providing a second copy of the Vilspa images on tape. We thank M. Begelman, M. Donahue, A. Lawrence, F. Makino, D. Maoz, E. Rosenblatt, A. Sadun, P. Smith,

W.-H. Sun, E. Tanzi, and H. C. Thomas for their support of this project, and the IUE Peer Review Panel for its generous allocation of time. C. M. U. acknowledges Rick Shafer and Jerry Kriss for helpful discussions about error analysis, and Max Camenzind and Gopal Krishna for helpful discussions about the interpretation. We thank Jay Lockman for providing H I measurements toward PKS 2155−304 in advance of publication. This work was supported in part by NASA grant NAG 5-1034. A. V. F. acknowledges support from NSF grant AST-8957063 and NASA grant NAG 5-1800.

REFERENCES

Allen, R. G., Smith, P. S., Angel, J. R. P., Miller, B. W., Anderson, S. F., & Margon, B. 1993, ApJ, 403, 610
Barylak, M., Wasatonic, R., & Imhoff, C. 1984, ESA *IUE* Newsletter, 20, 201
Bevington, P. R. 1969, Data Reduction and Error Analysis for the Physical Sciences (New York: McGraw-Hill), 169
Blandford, R., & Rees, M. J. 1978, in Pittsburgh Conference on BL Lac Objects, ed. A. M. Wolfe (Pittsburgh: Univ. of Pittsburgh), 328
Bohlin, R. 1988, NASA, *IUE* Newsletter, 35, 141
Bohlin, R., & Grillmair, C. J. 1988, ApJS, 68, 487
Bohlin, R., Harris, A. W., Holm, A. V., & Gry, C. 1990, ApJS, 73, 413
Bowyer, S., Brodie, J., Clarke, J. T., & Henry, J. P. 1984, ApJ, 278, L103
Brinkmann, W., et al. 1993, in preparation
Camenzind, M., & Krockenberger, M. 1992, A&A, 255, 59
Canizares, C. R., & Kruper, J. S. 1984, ApJ, 278, L99
Carini, M., & Miller, H. R. 1992, ApJ, 385, 482
Carrasco, L., Dultzin-Hacyan, D., & Cruz-Gonzalez, I. 1985, Nature, 314, 146
Cassatella, A., Lloyd, C., & Riestra, G. 1988, NASA IUE Newsletter, 35, 225
Celotti, A., Maraschi, L., & Treves, A. 1991, ApJ, 377, 403
Clavel, J., et al. 1991, ApJ, 366, 64
Courvoisier, T., et al. 1993, in preparation
Crenshaw, M. D., Bruegman, O. W., & Norman, D. J. 1990, PASP, 102, 463
Edelson, R. A. 1992, ApJ, 401, 516
Edelson, R. A., et al. 1991, ApJ, 372, L9
Edelson, R. A., et al. 1993, in preparation
Edelson, R. A., & Krolik, J. H. 1988, ApJ, 333, 646
Edelson, R., Pike, G. F., Saken, J. M., Kinney, A., & Shull, J. M. 1992, ApJS, 83, 1
Elvis, M., Lockman, F. J., & Wilkes, B. J. 1989, AJ, 97, 777
Fabian, A. C. 1979, Proc. R. Soc. Lond., A, 366, 449
Falomo, R., Giraud, E., Maraschi, L., Melnick, J., Tanzi, E. G., & Treves, A. 1991, ApJ, 380, L67
Feigelson, E., et al. 1986, ApJ, 302, 337
Finley, D., et al. 1993, in preparation
George, I. M., Warwick, R. S., & Bromage, G. E. 1988, MNRAS, 232, 793
Ghisellini, G., Maraschi, L., & Treves, A. 1985, A&A, 146, 204
Holm, A. V., & Crabb, W. G. 1979, NASA IUE Newsletter, 7, 40
Hutter, D. J., & Mufson, S. L. 1986, ApJ, 301, 50
Kinney, A. L., Bohlin, R. C., & Neill, J. D. 1991, PASP, 103, 694
Königl, A. 1981, ApJ, 243, 700
Lockman, F. J., Jahoda, K., & McCammon, D. 1986, ApJ, 302, 432
Lockman, F. J., & Savage, B. D. 1993, in preparation
Madejski, G. 1985, Ph.D. thesis, Harvard Univ.
Malina, R. F., & Bowyer, C. S. 1992, EUVE Newsletter, Vol. 2, No. 6
Maraschi, L., Tagliaferri, G., Tanzi, E. G., & Treves, A. 1986, ApJ, 304, 637
Marscher, A. P. 1980, ApJ, 235, 386
Morini, M., et al. 1986, ApJ, 306, L71
Mufson, S. L., Hutter, D. J., Kondo, Y., Urry, C. M., & Wiśniewski, W. Z. 1990, ApJ, 354, 116
Ostriker, J. P., & Vietri, M. 1985, Nature, 318, 446
———. 1990, Nature, 344, 45
Padovani, P., & Urry, C. M. 1990, ApJ, 356, 75
Perez, M., & Loomis, C. 1991, Record of the Meeting of the International Ultraviolet Explorer User's Committee (CSC/TM-91/6142), p. I-3
Pounds, K. A., Allen, D. J., Barber, C., Barstow, M. A. 1992, MNRAS, in press
Press, W. 1978, Comm. Astrophys., 7, 103
Quirrenbach, A., Witzel, A., Krichbaum, T. P., Hummel, A., Alberdi, A., & Schalinski, C. 1989, Nature, 337, 442
Quirrenbach, A., et al. 1991, ApJ, 372, L71
Schneider, P., & Weiss, A. 1987, A&A, 171, 49
Seaton, M. J. 1979, MNRAS, 187, 73P
Sembay, S., Warwick, R. S., Urry, C. M., Sokoloski, J., George, I. M., Makino, F., Ohashi, T., & Tashiro, M. 1992, ApJ, 404, 112
Shull, J. M., & Van Steenberg, M. 1985, ApJ, 294, 599
Smith, P. S., & Sitko, M. L. 1991, ApJ, 383, 580
Smith, P. S., Hall, P. B., Allen, R. G., & Sitko, M. L. 1992, ApJ, 400, 115
Snyder, W. A., et al. 1980, ApJ, L11
Stark, A. A., Gammie, C. F., Wilson, R. W., Bally, J., Linke, R. A., Heiles, C., & Hurwitz, M. 1992, ApJS, 79, 77
Stickel, M., Fried, J. W., & Kühr, H. 1988, A&A, 191, L16
Stickel, M., Padovani, P., Urry, C. M., Fried, J. W., & Kühr, H. 1991, ApJ, 374, 431
Teays, T., & Garhart, M. 1990, NASA IUE Newsletter, 41, 94
Treves, A., et al. 1989, ApJ, 341, 733
Ulrich, M.-H., Hackney, K. R. H., Hackney, R. L., & Kondo, Y. 1984, ApJ, 276, 466
Urry, C. M., Kondo, Y., Hackney, K. R. H., & Hackney, R. L. 1988, ApJ, 330, 791
Urry, C. M., & Mushotzky, R. F. 1982, ApJ, 253, 38
Urry, C. M., & Reichert, G. A. 1988, NASA IUE Newsletter, 34, 95
Wagner, S., & Witzel, A. 1992, in Extragalactic Radio Sources, ed. J. Roland, H. Sol, & G. Pelletier (Cambridge: Cambridge Univ. Press), 59
Walter, R., & Courvoisier, T. J.-L. 1991, A&A, 250, 312
Wambsganss, J., Paczyński, B., & Katz, N. 1990, ApJ, 352, 407
Wandel, A., & Urry, C. M. 1991, ApJ, 367, 78
Worrall, D. M., et al. 1986, ApJ, 303, 589